

DYNAMIC MEASUREMENTS WITH A LUMINESCENT
PHOTOELASTIC COATING

by

MELISSA LYNN CONWAY

DR. JAMES P. HUBNER, COMMITTEE CHAIR
DR. JIALAI WANG
DR. STANLEY E. JONES

A THESIS

Submitted in partial fulfillment of the requirements for the degree
of Master of Science in the Department of Aerospace
Engineering and Mechanics in the Graduate
School of The University of Alabama

TUSCALOOSA, AL

2012

Copyright Melissa Lynn Conway 2012

ALL RIGHTS RESERVED

ABSTRACT

The luminescent photoelastic coating (LPC) technique optically measures full-field, in-plane strain and principal strain directions on specimens of interest. Typically, a circularly-polarized, continuous, blue-light source is used to excite the coating. The resulting emission polarization, and, hence, emission intensity when viewed through an analyzer optic, is a function of the absorption, luminescence, and surface strain. This research thesis focuses on the dynamic application of the technique, specifically cyclic-load cases as the image intensity is too low for the camera to accurately capture transient-load cases. The dynamic tests involved bar specimens and square-tube specimens loaded at 1 Hz and 10 Hz. Instead of continuous excitation, strobed excitation was phase-synchronized with the frequency of the specimen. The experimental set-up and results are discussed.

DEDICATION

I dedicate this thesis to my parents, Randall and Brenda Conway, who have always set a great example for me and taught me the importance of working hard.

LIST OF ABBREVIATIONS AND SYMBOLS

A	amplitude of the light vector
A_t	light vector
A_{t1}	component of light through fast axis (axis 1)
A_{t2}	component of light through slow axis (axis 2)
a	maximum amplitude of the light vector
a_b	absorptivity
C	relative stress-optic coefficient
$C3D8$	8-noded linear brick element in <i>Abaqus</i>
C_1	stress-optic coefficient of axis 1
C_2	stress-optic coefficient of axis 2
c	speed of light propagation
CCD	charge-coupled device
d_1	distance from point of application of load to pixel 1
d_2	distance from pixel 1 to pixel 2, corresponding to target points
E	Young's Modulus
F	amplitude of optical strain response
FEA	finite element analysis
F_g	gage factor
F_ε	coating fringe value in terms of strain
F_σ	coating fringe value in terms of stress

f	frequency of the light
f_ε	material fringe value in terms of strain
f_σ	material fringe value in terms of stress
G	phase of optical strain response
g	gain
h	thickness of doubly refracting plate
h_c	thickness of the photoelastic coating
I	emission intensity at a given analyzer angle
I_{avg}	average emission intensity over sequence of analyzer angles
I_{\parallel}	intensity of the image with analyzer and linear polarizer parallel
I_{\perp}	intensity of the image with analyzer and linear polarizer perpendicular
K	optical sensitivity coefficient
L	length from point of load application to the clamped end
LED	light emitting diode
LPC	luminescent photoelastic coating
N	number of complete cycles of relative retardation
n_a	index of refraction of air
n_c	index of refraction of the coating
n_1	index of refraction of axis 1
n_2	index of refraction of axis 2
OSR	optical strain response
POA	point of application
P_{y1}	y coordinate for pixel 1
P_{y2}	y coordinate for pixel 2
QWP	quarter-wave plate

R_i	resistance in instrumentation amplifier ($i=G, 1, 2, \text{ or } 3$)
r	anisotropy of the coating
T	period of a harmonic function
t	time
t_s	thickness of the specimen
V_{avg}	average voltage
V_{in}	input voltage
V_{max}	maximum voltage
$V_{trigger}$	trigger voltage
V_{out}	output voltage
x	distance from the point of application of load
x, y, z	coordinate system
x', y', z'	coordinate system after rotating about the x axis by angle ψ'
z	axis of propagation of light
$2D$	two-dimensional
$3D$	three-dimensional
α	analyzer angle
β	angle between light vector and axis 1
γ	maximum shear strain
γ_{eff}	effective maximum shear strain
$\gamma_{eff,p}$	effective maximum shear strain for parallel incidence
$\gamma_{eff,o}$	effective maximum shear strain for oblique incidence
$\gamma_{max,p}$	maximum in-plane shear strain for parallel incidence
$\gamma_{max,o}$	maximum in-plane shear strain for oblique incidence

γ_{xy}	shear strain in the xy plane
γ_{yz}	shear strain in yz plane
$\varepsilon_{desired}$	desired strain level
ε_{max}	maximum strain level
ε_x	axial strain
ε_y	lateral strain
ε_z	normal strain
ε_1	primary in-plane principal strain
ε_2	secondary in-plane principal strain
ε_3	out-of-plane principal strain
ε^s	strain at the specimen surface
ε^c	strain in the coating
η	coating calibration coefficient
δ	relative retardation
δ_d	deflection of beam
δ_1	retardation of axis 1
δ_2	retardation of axis 2
λ	wavelength of light
λ_{em}	emission wavelength
λ_{ex}	excitation wavelength
λ^*	effective wavelength, $\lambda_{em}\lambda_{ex}/(\lambda_{em} + \lambda_{ex})$
$\tilde{\lambda}_{em}$	effective excitation wavelength, λ_{em}/λ^*
$\tilde{\lambda}_{ex}$	effective excitation wavelength, λ_{ex}/λ^*
v	Poisson's ratio

v^c	Poisson's ratio of the coating
σ_x	stress in the x direction
σ_z	normal stress
σ^s	stress at the specimen surface
σ^c	stress in the coating
σ_1	primary in-plane principal stress
σ_2	secondary in-plane principal stress
τ_{xz}	shear stress in the xz plane
τ_{yz}	shear stress in the yz plane
ϕ	polarization efficiency
ψ	oblique excitation angle
ψ'	oblique excitation angle within the coating

ACKNOWLEDGEMENTS

I would like to express my greatest appreciation for my advisor, Dr. James P. Hubner, for his patience, guidance, and teaching. He has given me opportunities I likely never would have had and has supported me along the way. I would also like to thank Dr. Stanley Jones and Dr. Jialai Wang for serving on my committee. I am greatly indebted to Mr. Hisham Ali for the countless hours he put in to help my research. I would like to thank Mr. Daniel Gerber for training and helping me on this research. I also want to thank the Machine Shop for helping me with various tasks along the way. Thank you to Dr. Mark Barkey for his help with FEA modeling. Finally, I would like to thank all of my family and friends for their support.

CONTENTS

ABSTRACT.....	ii
DEDICATION	iii
LIST OF ABBREVIATIONS AND SYMBOLS	iv
ACKNOWLEDGEMENTS	ix
LIST OF TABLES.....	xii
LIST OF FIGURES	xiii
INTRODUCTION	1
BACKGROUND AND THEORY OF PHOTOLEASTICITY	5
2.1 History	5
2.1.1 Photoelasticity	5
2.1.2 Photoelastic Coating	6
2.1.3 Strain Separation.....	7
2.2 Properties of Light and Theory of Photoelasticity	8
2.2.1 Properties of Light	8
2.2.2 Polarized Light	9
2.2.3 Retardation Plates	11
2.2.4 Polariscopes	13
2.2.5 The Stress-Optic Law	15
LUMINESCENT PHOTOLEASTIC COATING.....	17
3.1 Introduction	17
3.2 Coating Formulation and Application.....	18
3.3 Experimental Setup	19
3.3.1 Excitation Source.....	19
3.3.2 Digital Camera.....	20
3.3.3 Triggering Circuit	20
3.4 Theory of Operation	25
EXPLANATION OF LAB EQUIPMENT AND COATING PROCEDURE.....	29
4.1 Luminescent Imaging Lab.....	29
4.1.1 LED Lamp	29

4.1.2 CCD Camera.....	31
4.1.3 Analyzer Rotation Stage	32
4.1.4 Optics.....	33
4.1.5 Motor and Variable Drive.....	34
4.1.6 Timing Circuit Components	35
4.1.7 Oscilloscope.....	35
4.1.8 Voltage Generators	36
4.1.9 Bending Apparatus	36
4.1.10 Software.....	37
4.1.11 Specimens	42
4.2 Coating Preparation Lab.....	43
4.2.1 Balances.....	43
4.2.2 Coating Thickness Instrument	43
4.2.3 Fume Hood	43
4.2.4 UV Lamps.....	44
4.3 Coating Technique	45
STRAIN SEPARATION RESULTS AND DISCUSSION.....	47
5.1 Image Acquisition and Processing	47
5.2 Theoretical Modeling	49
5.3 Measured Coating Calibration Parameters: \square and \square	55
5.4 Rosette Strain Gage Data	56
5.5 Experimental Results.....	57
5.5.1 Test Conditions.....	57
5.5.2 Experimental OSR.....	60
5.5.3. Experimental Strain Separation	66
5.5.5. Phase Results	71
CONCLUSIONS.....	73
REFERENCES	75

LIST OF TABLES

Table 1.0. Test matrix for all tests conducted.....	4
Table 2.1 Four combinations of optical elements for circular polariscope [7].....	15
Table 5.1. Calibration coefficients for each specimen.....	55
Table 5.2. 95% precision interval values for 3D specimens at parallel and oblique incidence angles.	56
Table 5.3. Image acquisition parameters for various specimen types and load states.....	59
Table 5.4. Sensitivity of parameters.	61

LIST OF FIGURES

Fig. 1.0. Camera, lamp and specimen positions.	3
Fig. 2.1. Amplitude of a light vector as it propagates along the z axis [7].	8
Fig. 2.2. Motion of light vector for (a) plane, (b) circularly, and (c) elliptically polarized light [7].	10
Fig. 2.3. Unpolarized light passing through a linear polarizer and creating linearly (or plane) polarized light [8].....	11
Fig. 2.4. Linear polarizer and quarter wave plate in series to create circularly polarized light [8].	12
Fig. 2.5 Plane polarized light vector passing through a doubly refracting plate [7].....	12
Fig. 2.6. Circular transmission polariscope [7].....	14
Fig. 3.1: Visualization of penetration depth due to the absorption dye in the coating [2].....	18
Fig. 3.2. Linear polarizer and quarter wave plate diagram [8].	19
Fig. 3.3: Experimental setup diagram [13].	20
Fig. 3.4. Instrumentation amplifier circuit diagram.....	21
Fig. 3.5. Screenshot of LabVIEW program used to update reference voltage of the comparator.	23
Fig. 3.6: Trigger network diagram.....	25
Fig. 3.7. Theoretical relationship between emission intensity and analyzer angle.....	27
Fig. 3.8. Time-dependent photosensor (coating) and strain gage response during 10 Hz dynamic loading [12].....	29
Fig. 3.9. Root-mean-square (rms) amplitude of the respective signals at the measured peak-frequency.....	30
Fig. 4.1. (a) Published [14] spectral measurement and (b) measured spectral emission of LEM2X-DM [2].....	30
Fig. 4.2. Published plot of a 4-ms trigger signal and the LEM2X-DM response [14].	31
Fig. 4.3. Quantum Efficiency of different PIXIS 1024 CCD cameras [15].....	32
Fig. 4.4. Image of the excitation source imaging setup.	33
Fig. 4.5. Emission spectrum of luminescent photoelastic coating [2].	34
Fig. 4.6. Image of Rigol DS1052E Digital Oscilloscope.....	36
Fig. 4.7. Reaction beam used to clamp one end of a specimen.	37

Fig. 4.8. Screenshot of LabVIEW program used to control variable drive.	38
Fig. 4.9. Screenshot of LabVIEW program used to update the reference voltage for the comparator.	39
Fig. 4.10. Screenshot of program used to acquire images.	40
Fig. 4.11. Screenshot of program used to analyze images.	41
Fig. 4.12. Coated specimens.	42
Fig. 4.13. Air Sentry high performance fume hood.	44
Fig. 4.14. High-intensity ultraviolet light used to cure the specimens.	45
Fig. 5.1. Diagram showing variable definitions to convert pixels to inches.	50
Fig. 5.2. Diagram showing oblique excitation and the plane rotation.	52
Fig. 5.5. Lamp, camera, and specimen positions and orientations (a) and test instrumentation (b).	58
Fig. 5.6. Region of lamp flash on the sinusoidal strain response of cyclically loaded specimen.	60
Fig. 5.7. Parallel and oblique OSR images for the 2D specimen.	61
Fig. 5.8. OSR parallel and oblique images for (a) front and (b) side of a 3D specimen.	63
Fig. 5.9. Parallel (top) and oblique (bottom) excitation OSR response along the tension-side centerline of the 2D bar.	64
Fig. 5.10. Parallel (top) and oblique (bottom) excitation OSR response along the tension-side centerline of the square-tube beams.	65
Fig. 5.11. Separated principal strains for the 2D bar specimen.	66
Fig. 5.12. 8-noded linear brick element.	67
Fig. 5.13. Principal strain in the axial direction.	68
Fig. 5.14. Separated principal strains for the 3D beam specimen. Note: ABAQUS coordinate system used.	69
Fig. 5.15. Principal strains along (a) the width of the beam and (b) the depth of the beam.	70
Fig. 5.16. Phase plots of the front and side face of a 3D specimen in (a) color and (b) black and white.	72

INTRODUCTION

To be used safely in commercial applications, a structural component must be strong enough to withstand the predicted applied loads. Strain measurements assist a structural engineer to assess the stress state, hence strength, a structural component is experiencing due to external loading. Strain measurements allow a sample to be characterized and examined, determining yield and failure values and locating stress concentrations.

Stress tests are conducted on materials to verify that they meet specific design criteria. These tests use either pointwise or full-field techniques. There will be advantages and disadvantages of each measurement technique, and the appropriate technique may vary based on the specimen. Strain gages, an extremely common-place, accurate and pointwise technique, cannot match the spatial resolution of full-field techniques. Additionally, applying strain gages can be a cumbersome and difficult task on complex components. Luminescent photoelastic coating method is a developing full-field technique that can optically measure in-plane maximum shear strain and principal strain directions. While LPC has higher spatial resolution than strain gages, the accuracy of strain gages surpasses that of LPC.

LPC is composed of a photoelastic binder, an absorption dye, and a luminescent dye. In a completely dark environment, the coating is excited by blue circularly polarized light from an LED lamp. The photoelastic binder retards the light while the absorption dye determines the penetration depth and eliminates thickness dependence. With the absorption dye, the coating does not need to be applied perfectly uniform as long as a minimum thickness is obtained. The

luminescent dye retains the polarization changes due to strain and emits light at a higher wavelength. The luminescence then is captured through an analyzer (a linear polarizer) by a CCD camera, and through image processing and calibration, the captured intensity images are converted to spatial maps of maximum in-plane shear strain and principal strain directions.

Oblique incidence excitation is used as a method to separate the principal strains at a point [1]. This approach has been extended to full-field measurements using an LPC [2, 3]. This method requires two sets of images to be acquired. One set of images is acquired with the lamp parallel to the camera facing the specimen. The other is acquired when the lamp is set at an angle relative to the camera. Each set of images produces data sensitive to the maximum shear strain in the plane perpendicular to the excitation path. The measured intensities differ due to the out-of-plane strain component present within the coating. As the maximum shear strain is simply the difference between the principal strains, these two sets of images act as two equations to solve for the two unknown principal strains, knowing coating calibration parameters. The images are analyzed and the strains are separated to determine the individual principal strains.

Static measurements have previously been completed on both 2D and 3D subjects [2, 3]. Thin aluminum bars were used as the 2D subjects and hollow circular tubes were used for 3D specimens. The results for 2D specimens were satisfactory and the research now pushes towards acquiring dynamic results of the coating. Gerber began work on the dynamic measurements for 2D specimens. There were errors in the experimental setup that prohibited acceptable results. The research has continued and applied to both 2D specimens and 3D with hollow rectangular aluminum tubes [12].

This thesis explores dynamic LPC's performance on two-dimensional (2D) and three-dimensional (3D) beam specimens undergoing cyclic loading. The excitation lamp strobes at a specified strain threshold level for durations of 2.5-25 ms, depending on the loading frequency of the specimen. The camera's shutter opens for an extended period of time, and from the flashes of the lamp, the camera captures repeated exposures of the specimen at one position in the cycle. The specimens of interest were imaged using parallel and oblique lamp positions to separate the principal strains. Fig. 1.0 shows the layout of the camera, lamp, and specimen positions.

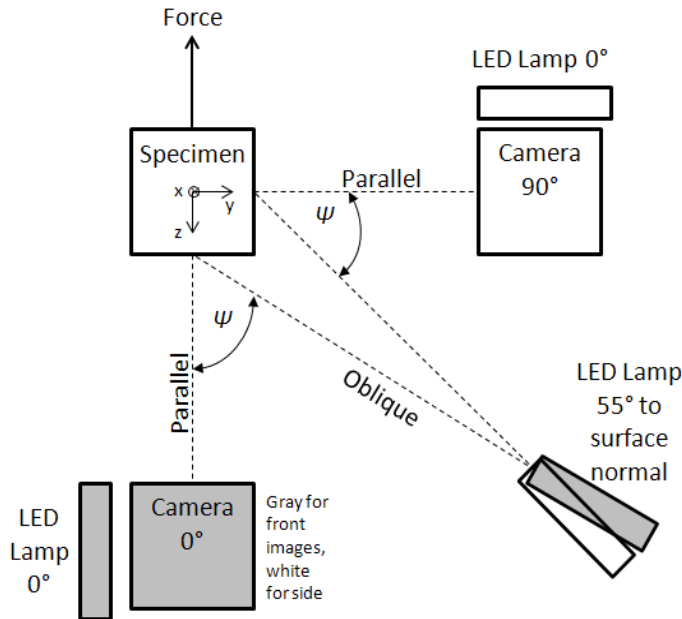


Fig. 1.0. Camera, lamp and specimen positions.

The objectives of this thesis are:

1. to develop a dynamic testing technique implementing an LPC coating to accurately obtain in-plane maximum shear strain and principal direction results and

2. to separate principal strains from the dynamic measurements of 2D and 3D specimens.

Tests were conducted on the beam specimens at frequencies of 1 Hz and 10 Hz; images were captured near the maximum deflection of the specimens. Two different camera positions were used as well as two LED positions for each camera position. Table 1.0 outlines the parameters for each test condition and shows the effective strain state the camera acquired.

Table 1.0. Test matrix for all tests conducted.

Specimen Type	Frequency	Effective Excitation Time	Effective Strain State Acquired
[]	[Hz]	[s]	[$\mu\epsilon$]
2D Bar	1	13.5	521.6 ± 2.5
	10	13.5	521.6 ± 2.5
3D Beams	1	13.5	523.5 ± 2.5
	10	13.5	523.5 ± 2.5

Chapter 2 includes information regarding the history and early theory of photoelasticity as well as light properties relevant to understanding the technique. An in-depth look at how the luminescent photoelastic coating technique is used for this experiment is discussed in Chapter 3. This chapter also discusses the basic experimental setup. All lab equipment and software used is detailed in Chapter 4. Chapter 5 presents and discusses strain separation and principal strain direction results from the dynamic tests, and, finally, Chapter 6 draws conclusions and outlines future work.

BACKGROUND AND THEORY OF PHOTOELASTICITY

2.1 History

2.1.1 Photoelasticity

Photoelasticity is an experimental technique used to measure strains of an object experiencing an applied or residual load. This object must be either a photoelastic model or a model with a photoelastic coating. These photoelastic models begin as isotropic; they have the same index of refraction at every point when free of stress. As the object is loaded, the material becomes anisotropic, and the index of refraction is no longer identical at every point. Sir David Brewster and Thomas Seebeck in the early 1800s observed that the models become doubly refracting when a load is applied and this behavior serves as the basis for photoelasticity [4].

Seebeck was heavily involved in optics research from 1802-1820. He primarily researched photoelasticity in glass. Seebeck investigated how heating and cooling glass affected its birefringence by observing the glass specimens through crossed and parallel polariscopes. He observed that when glass was cooled down slowly, it did not exhibit birefringence. Glass that was cooled down quickly showed interference fringes. He also revealed that glass did not show birefringence at high temperatures. Thus, he concluded that observing a glass article through polarized light could reveal how quickly it was cooled down. This was characteristic of the basic photoelastic effect, isoclinic and interference fringes [4].

Malus discovered that light could possibly be polarized from reflection of a glass plate and studied birefringence in mediums including crystals and thin slices of plant and animal tissues. Biot observed that when light passes obliquely through a pile of glass plates, the light becomes polarized [4].

Maxwell reported on the relationship between the change in the index of refraction of a doubly refracting material and stress in 1853. He determined that the changes observed in the index of refraction were linearly proportional to the strains experienced by the specimen. This theory is known as the stress-optic law and is fundamental to the understanding of photoelasticity [5].

Photoelasticity is typically divided into two categories; two- and three-dimensional. If the body can be characterized by plane strain, then two-dimensional methods are used. Otherwise, three-dimensional methods are used that can be time consuming and difficult [5].

2.1.2 Photoelastic Coating

Traditional reflective photoelastic coatings can be employed in conjunction with the theory of photoelasticity to provide a measure of full-field strain. These coatings must have some type of reflective attribute to capture the strain pattern. The technique has been effective in the past and new techniques are still being researched [6].

The optical response of a photoelastic coating depends on the coating properties and the tool used to measure the response. The coatings are sensitive to the principal strain directions as well as the difference in principal strains. For example, when a coating is measured by a plane reflection polariscope, two sets of patterns are observed. These are called isoclinic and isochromatic fringes. The isoclinic fringes indicate the principal stress directions and the isochromatic indicate the difference in principal stresses in the coating [7].

2.1.3 Strain Separation

Often it is desirable to determine the principal strains from photoelastic models. There are several methods that can be used to separate the principal strains and they include the lateral-extensometer method, integration methods, mathematical solution of Laplace's equation, oblique incidence of light method [9], strip coatings [7], and thermoelasticity [10]. The lateral-extensometer method is not applicable to photoelastic coatings [9] and the integration methods are only applicable to two-dimensional plane-stress problems [7]. The oblique incidence method is potentially the easiest full-field, 3D technique to employ in an experimental environment.

The oblique incidence method involves acquiring two sets of image data that do not correspond to the same plane of propagation of light; traditionally this rotation to a different plane is about a known principal axis. However, with the LPC technique, this is not required [3]. The method has been proven to give accurate results and can be more easily performed when the principal stresses are significant [1].

Two sets of data are needed to separate the principal strains. These two data sets are used to solve two linear equations with the two unknown principal stresses. Typically, one set of data, derived from imaging, is acquired when the excitation source and the observer are parallel to each other. The next data set is acquired when either the observer or the excitation source is rotated about one of the principal axes of stress. By rotating either the excitation source or the observer, an independent data set is acquired. This rotated data set is termed the "oblique" set. There will be a difference in the measured optical strain response between the two sets of data as the optical response is dependent upon the plane perpendicular to the propagation and the oblique set will have information relating to the surface-normal (or out-of-plane) strain component [9].

Takahashi and Hubner [11] showed that the oblique-incident optical response for a luminescent photoelastic coating was unique from the normal-incident optical response on a three-dimensional model. This distinctiveness was due to this difference in the out-of-plane strain component within the coating between the oblique and normal responses. This demonstrated the possibility of applying the oblique-incidence method to three-dimensional models.

2.2 Properties of Light and Theory of Photoelasticity

2.2.1 Properties of Light

Light is an electromagnetic disturbance that propagates through space and forms an electromagnetic wave. This wave can be modeled as a sinusoidal function where the amplitude of the light vector, A , is a function of the position along the axis of propagation, z , time, t , speed of light propagation, c , wavelength, λ , and maximum amplitude, a [7]. Fig. 2.1 is an illustration of the changing amplitude of the light vector.

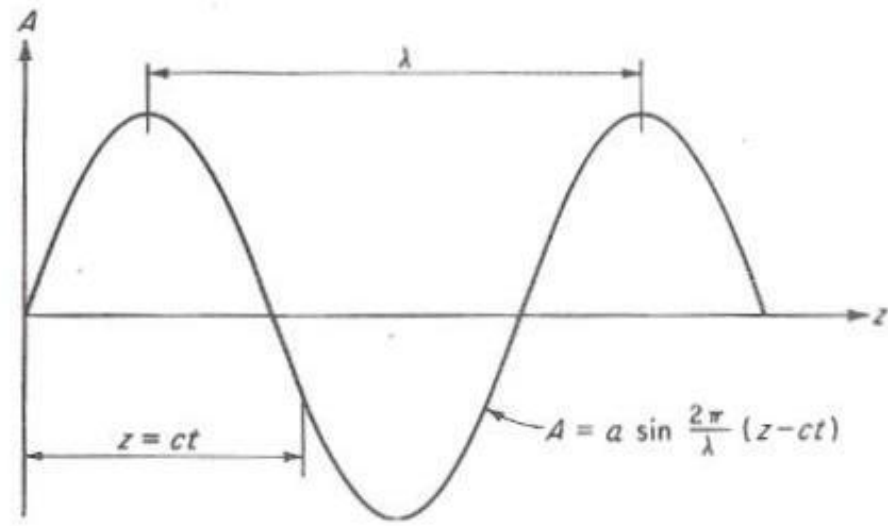


Fig. 2.1. Amplitude of a light vector as it propagates along the z axis [7].

The wavelength is the distance between peaks of the function shown in Fig. 2.1. The wavelength of a light wave indicates the color of the light. Visible light ranges in wavelength from violet at 380 nm to red at 750 nm. Equation (2.1) is the relationship between the period, T , of the function, the wavelength of the light, and velocity of propagation [7],

$$T = \frac{\lambda}{c}. \quad (2.1)$$

The frequency of the light wave is the rate of oscillations per second. It is given by,

$$f = \frac{1}{T}. \quad (2.2)$$

2.2.2 Polarized Light

Unpolarized light vibrates in all directions perpendicular to the plane of propagation. Light can be polarized to vibrate in one direction or vibrate uniformly to create a circular helix or elliptical helix in the direction of propagation. These are referred to as plane polarized light, circularly polarized light, and elliptically polarized light, respectively. Plane polarized light is produced from a linear polarizer. Circularly and elliptically polarized light are created through a sequence of a linear polarizer and a retardation plate. These three types of polarized light are illustrated in Fig. 2.2 [7].

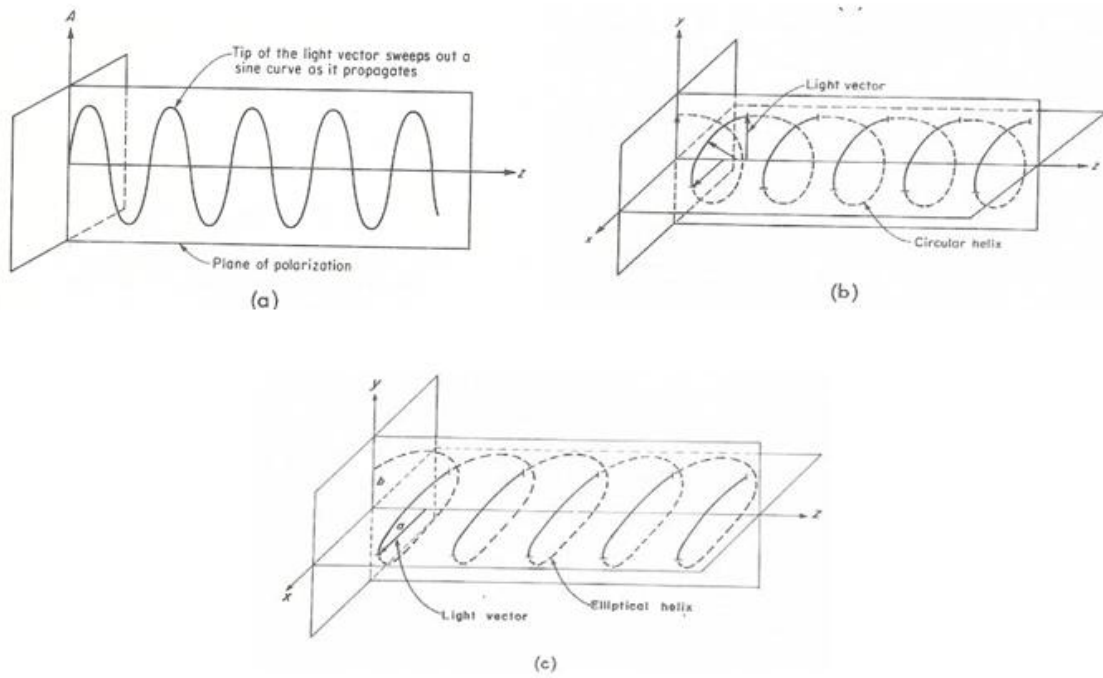


Fig. 2.2. Motion of light vector for (a) plane, (b) circularly, and (c) elliptically polarized light [7].

Linear polarizers only allow the component of light parallel to the axis of polarization to pass through the plate [7]. This creates plane polarized light where all of the components of the light vector lie in the plane of polarization, and there is a reduction in light intensity (Fig. 2.3).

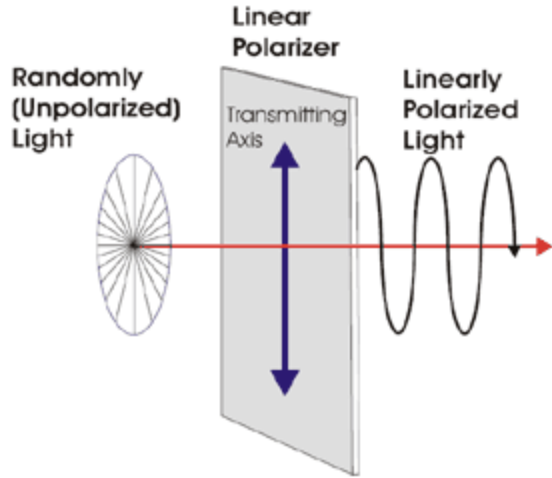


Fig. 2.3. Unpolarized light passing through a linear polarizer and creating linearly (or plane) polarized light [8].

2.2.3 Retardation Plates

A retardation plate has the ability to split a light vector into two orthogonal components and, then, “retard” or slow down one of the components relative to the other. This property is known as doubly refracting. Crystals and stressed plastics also exhibit this property. If a retardation plate is placed in front of plane polarized light, it will either create elliptically or circularly polarized light. Circularly polarized light is created from a relative retardation of $\lambda/4$. The $\lambda/4$ retardation plate is termed a quarter-wave plate (QWP). A retardation plate that retards one light component by any other relative amount, will create elliptically polarized light or linearized if the QWP axis is aligned with the linear polarizer axis. Fig. 2.4 is a visual for creating circularly polarized light from unpolarized light [7].

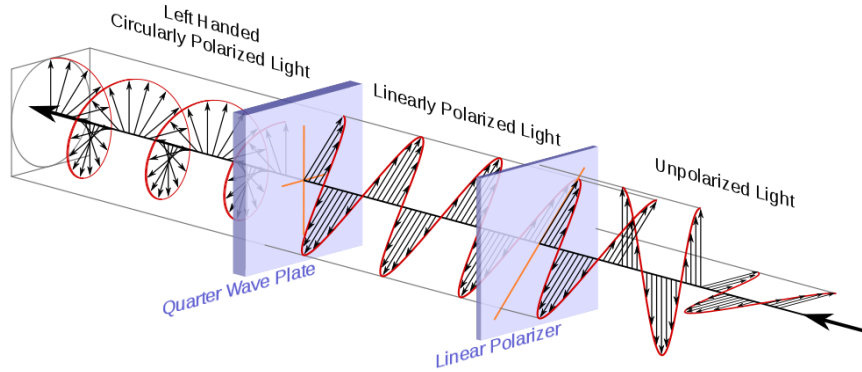


Fig. 2.4. Linear polarizer and quarter wave plate in series to create circularly polarized light [8].

A doubly refracting plate has two orthogonal principal axes that allow light to propagate through the medium at different velocities. The axis that transmits light faster is called the fast axis and the other, the slow axis. Suppose there is plane polarized light where the light vector is A_t . This light vector makes an angle, β , with the fast axis and is thus resolved into two components, A_{t1} and A_{t2} . A_{t1} is the component of light propagating through the fast axis and A_{t2} the slow axis. The A_{t2} component is described as being retarded relative to the A_{t1} component. Fig. 2.5 displays a retardation plate and the transmitted components [7].

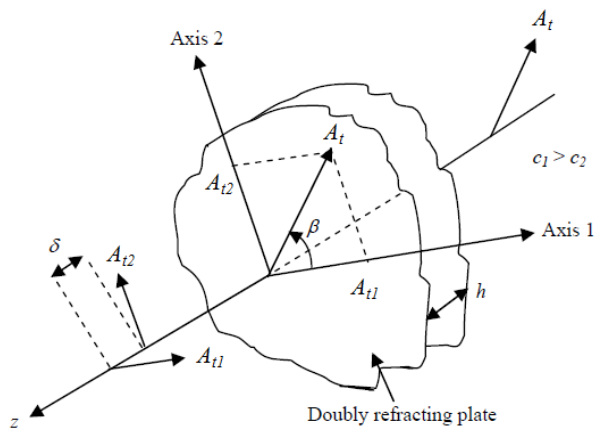


Fig. 2.5 Plane polarized light vector passing through a doubly refracting plate [7].

The resulting components can be visualized as a phase shift between the two sinusoidal functions. The relative retardation, δ , is related to the thickness of the plate, h , and the index of refraction associated with axes 1 and 2, n_1, n_2 [7],

$$\delta = \delta_1 - \delta_2 = h(n_1 - n_2). \quad (2.3)$$

When this relative retardation is $\lambda/4$, $\lambda/2$, or λ , the doubly refracting plate is called a quarter-wave, half-wave, and full-wave, respectively. Both the amplitude and the angle of rotation of the emerging light can be controlled by the plate [7].

2.2.4 Polariscopes

Polariscopes are optical arrangements used to characterize an object by the way it changes light waves. There are two typically employed polariscopes in photoelasticity: plane and circular. Plane and circular polariscopes can be arranged in either a transmission polariscope or a reflection polariscope. The orientations of the elements in the circular polariscope can create four different possibilities, each yielding either a dark or light field. [7].

2.2.4.1 Plane Polariscopes

The plane transmission polariscope consists of two linear polarizers and a light source. The components are aligned in series beginning with the light source, the linear polarizer, the specimen, and finally the analyzer (second linear polarizer). The plane reflection polariscope involves a specimen that has reflective qualities associated with it to reflect the transformed light. These polariscopes are arranged with a light source, linear polarizer, and the specimen in series. The specimen is able to reflect the light that has been changed by the model where it is able to pass through the analyzer to the observer. These polariscopes can also involve mirrors to change the direction of light for either the exciting or emitting light. The two linear polarizers

always have crossed principal axes in the plane polariscope, creating a dark field. When stressed, the photoelastic specimen or coating will produce fringe patterns indicative of the stress field [7].

2.2.4.2 Circular Polariscopes

Circular polariscopes are similar to the plane polariscopes except for two quarter-wave plates added to the optical path. In the circular polariscope, the first quarter-wave plate is in series just after the first linear polarizer [7]. The second quarter-wave plate is located between the specimen and the analyzer (Fig. 2.6).

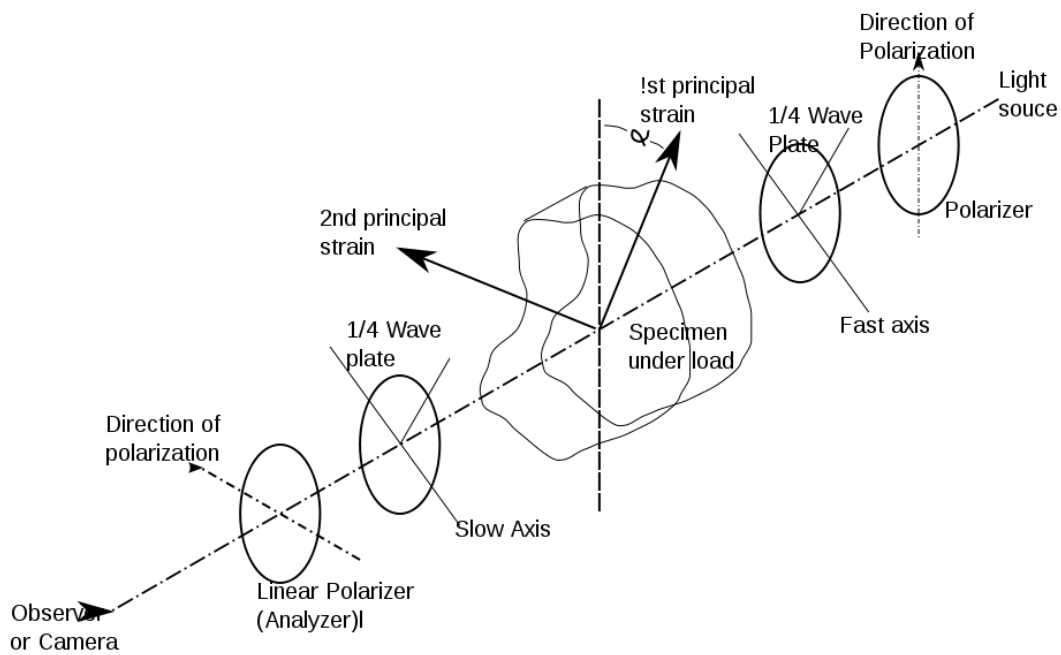


Fig. 2.6. Circular transmission polariscope [7].

Four orientations of the optical elements in the circular polariscope are possible by crossing different elements. These combinations create either a dark or light field [7]. The possibilities are shown in Table 2.1.

Table 2.1 Four combinations of optical elements for circular polariscope [7].

Arrangement	Quarter-wave Plates	Polarizer and Analyzer	Field
A	Crossed	Crossed	Dark
B	Crossed	Parallel	Light
C	Parallel	Crossed	Dark
D	Parallel	Parallel	Light

2.2.5 The Stress-Optic Law

The Stress-Optic Law is the basis for photoelasticity. Photoelasticity involves a photoelastic model or coating and a measurement technique to measure stress of the model. The photoelastic model or coating is isotropic prior to being stressed; meaning the index of refraction is uniform throughout the model or coating. As the model is stressed, the model becomes anisotropic with respect to its index of refraction. The model now acts as a doubly refracting plate. The principal stress axes are the same as the principal optical axes. The indexes of refractions along the two principal axes are dependent upon the magnitude of the principal stresses, σ_1 and σ_2 [7]. The relative index of refraction, $n_1 - n_2$, at a given point is given by (2.4),

$$n_1 - n_2 = (C_1 - C_2)(\sigma_1 - \sigma_2) = C(\sigma_1 - \sigma_2), \quad (2.4)$$

where $C = C_1 - C_2$ is the relative stress-optic coefficient. The relative retardation of the photoelastic model or coating is dependent on the thickness of the model or coating as well as the magnitude of the principal stresses (Eq. 2.5) [7],

$$\delta = hC(\sigma_1 - \sigma_2). \quad (2.5)$$

The more common way of writing the stress-optic law is,

$$\sigma_1 - \sigma_2 = \frac{Nf_\sigma}{h}, \quad (2.6)$$

where $N = \delta/\lambda$, the relative retardation in terms of a complete cycle, also called the fringe order, and $f_\sigma = \frac{\lambda}{c}$, the material fringe value. The light actually travels through the model twice when a birefringent coating is used. For this case, it can be written as,

$$\sigma_1^c - \sigma_2^c = \frac{Nf_\sigma}{2h_c} = NF_\sigma, \quad (2.7)$$

where $F_\sigma = f_\sigma/2h_c$ is the coating fringe value and the subscript c is used to refer to photoelastic coatings [7].

Photoelastic models can also help determine the difference in principal strains. Using Hooke's Law and substitutions from (2.7),

$$\varepsilon_1^c - \varepsilon_2^c = \left(\frac{1+\nu}{E}\right) \left(\frac{f_\sigma}{2h_c}\right) N = \left(\frac{f_\varepsilon}{2h}\right) N = F_\varepsilon N, \quad (2.8)$$

where $f_\varepsilon = \left(\frac{1+\nu}{E}\right) f_\sigma$, the material fringe value in terms of strain and $F_\varepsilon = \left(\frac{f_\varepsilon}{2h}\right)$, the coating fringe value in terms of strain [7].

LUMINESCENT PHOTOELASTIC COATING

3.1 Introduction

Luminescent photoelastic coating technique is a quantitative technique used to optically measure full-field strain with high spatial resolution. The coating is composed of three parts: a photoelastic binder, a luminescent dye and an absorption dye. The photoelastic binder retards light propagation as it passes through the coating depending on the stress state within the coating. The luminescent dye partially retains stress (or strain) induced polarization changes and emits light at a higher wavelength than the excitation. This enables the emission to be filtered from the excitation when capturing an image. The absorption dye limits the penetration depth of the excitation, enabling a thickness independent measure [12]. This is a desirable quality as it is difficult to apply the coating uniformly. A schematic of the excitation penetration depth is shown in Fig. 3.1.

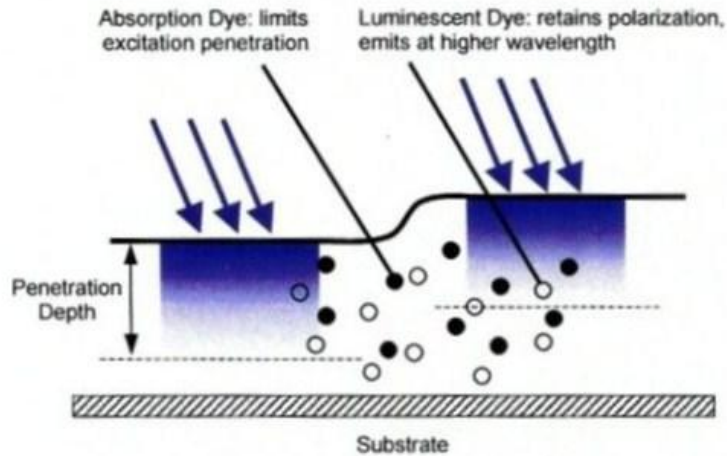


Fig. 3.1: Visualization of penetration depth due to the absorption dye in the coating [2].

3.2 Coating Formulation and Application

Two types of specimens were used in this experiment: 2D bar and 3D square tube. The specific amount of coating needed for each specimen is estimated using the surface area and thickness so as to spray a coating of at least 400 μm thick. There is also a 40-60% overspray correction added to the amount of coating. For the 2D beams, only 40% overspray is estimated. The 3D beams need a 60% overspray due to rotation of the specimen while coating. All of the components, except the luminescent and absorption dyes, of the LPC are mixed together and left stirring overnight. The next day the dyes are added and left to stir an additional few hours. All of the specimens, 2D and 3D, are anodized aluminum to reduce the emission reflection. They are lightly sanded and cleaned with acetone to ensure a suitable, clean surface for adhesion.

A small aerosol sprayer by Paasche, model H, is used to coat the specimens. Approximately 5ml of coating is sprayed for the first coat. The specimen is then flash cured under UV lamps for 10-15 minutes. Another coat is applied and then flash cured. The process continues until all of the coating is used. Flash curing is used to make certain the coating cures all the way through.

Otherwise, the coating will not adhere completely and complete strain transference from specimen to coating cannot be assumed.

3.3 Experimental Setup

3.3.1 Excitation Source

An LED lamp is used to excite the coating at approximately 460 nm. A linear polarizer and a quarter-wave plate are attached to the lamp. A linear polarizer only transmits the component of light parallel to the axis of polarization. The quarter-wave plate (QWP) is attached following the linear polarizer. This plate creates a quarter-wavelength phase shift between two perpendicular polarization components of the light wave when the QWP is 45° relative to the polarizer. The light becomes circularly polarized when passed through the linear polarizer and the quarter wave plate [7]. The QWP angle is set by monitoring the time-dependent excitation intensity passing through a spinning polarizer. When the intensity is constant (or near constant), the light is circularly polarized.

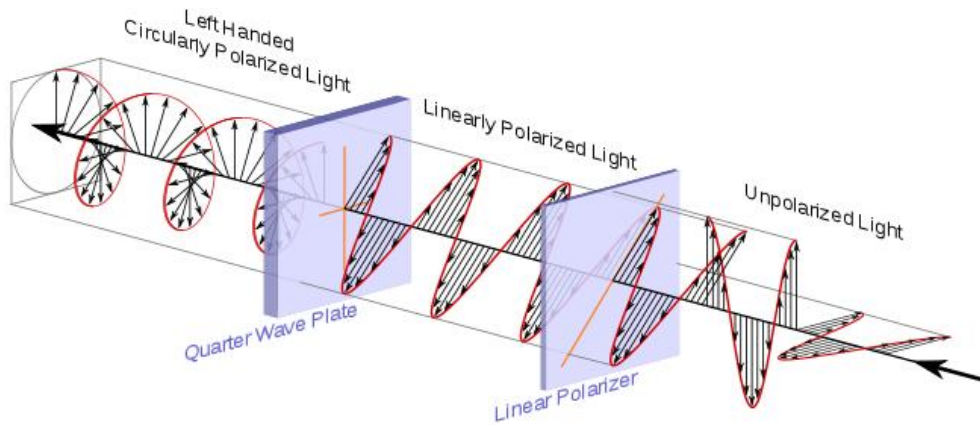


Fig. 3.2. Linear polarizer and quarter wave plate diagram [8].

3.3.2 Digital Camera

As the emitting light is captured by the camera, it passes through an analyzer, another linear polarizer, and an emission filter (Fig. 3.3). The emission filter allows only emission (orange light having a wavelength of approximately 600 nm) to pass through, keeping the reflecting blue light from being imaged. The camera itself is a charge-coupled device (CCD) with 16-bit dynamic resolution, high spatial resolution, and 1024 x 1024 pixels [2]. Images are acquired at 8 analyzer angles. The position of the analyzer is controlled by an in-house LabVIEW program, “LPC Acquisition.vi”. The user can save a sequence of images after specifying what angles to use.

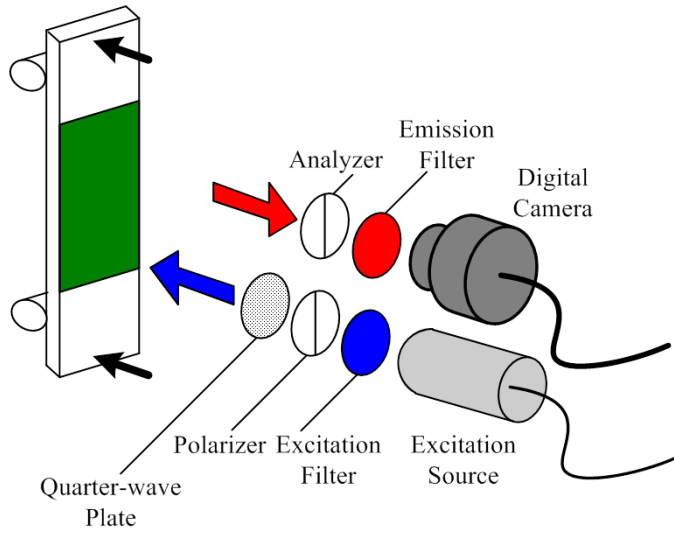


Fig. 3.3: Experimental setup diagram [13].

3.3.3 Triggering Circuit

An electronic circuit was developed to send a trigger pulse to the LED lamp when the aluminum cantilever beam undergoing harmonic motion is in a specific position of the cycle. A 120Ω strain gage mounted on the backside of the specimen was wired to a Wheatstone bridge (quarter-bridge configuration). The Wheatstone bridge measures an unknown resistance by balancing two legs of the circuit. One leg contains two 120Ω resistors and the other leg contains one 120Ω

resistor and an unknown resistor. The strain gage acts as the unknown resistor in this circuit given that it changes its resistance when stressed. The bridge is balanced when the strain gage is unstressed. The resistance change is proportional to the voltage output of the Wheatstone bridge. The voltage output of the Wheatstone bridge was approximately 8mV and needed to be amplified. This output voltage entered a series of LM741 op-amps arranged as an instrumentation amplifier shown in Fig. 3.4.

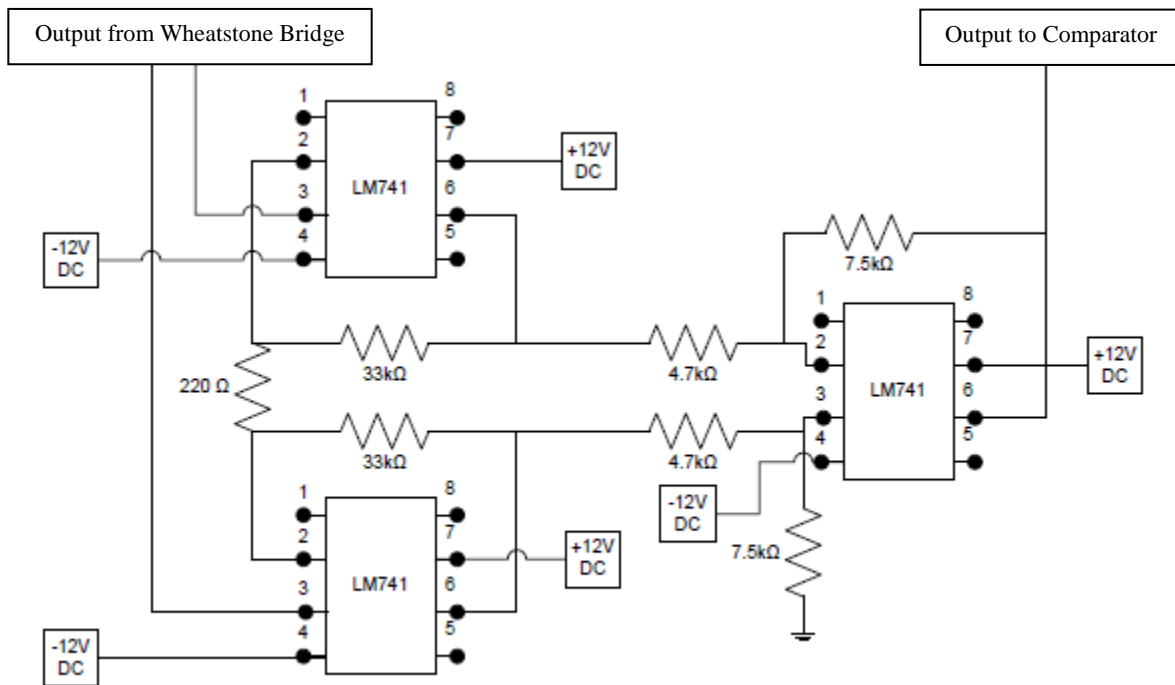


Fig. 3.4. Instrumentation amplifier circuit diagram.

The gain of the instrumentation amplifier was calculated by,

$$g = \frac{R_2}{R_1} \left(1 + \frac{2R_3}{R_G}\right), \quad (3.1)$$

where $R_1 = 4.6 \text{ k}\Omega$, $R_2 = 7.45 \text{ k}\Omega$, $R_3 = 26.9 \text{ k}\Omega$, and $R_G = 221 \Omega$. For the experiments, the calculated gain is approximately 400.

The output voltage of the Wheatstone bridge relative to the change in resistance of the strain gage is:

$$V_{out} = \frac{1}{4} \epsilon_x F_g V_{in} . \quad (3.2)$$

where ϵ_x is the axial strain, F_g is the gage factor for the strain gage, and V_{in} is the input voltage (12 V). At maximum deflection for the beam, about 0.3175 cm, the voltage output was calculated to be approximately .003697 V. Multiplied by the theoretical gain of the instrumentation amplifier, the maximum voltage output seen by the comparator should be approximately 1.464 V.

The voltage output from the instrumentation amplifier was passed into a comparator, comparing the input voltage to a designated reference voltage. When the input is higher than the reference, the comparator outputs the most negative voltage it can generate and when the input is lower, the output is the highest positive voltage that can be generated. The reference voltage that is chosen is specific to a particular location on the sinusoidal strain gage response. A negative side-effect of the system is that strain gage response drifts over time due to temperature effects, causing a drift in the true trigger strain value. The typical solution to this problem involves a “dummy” strain gage in a half-bridge configuration with the original strain gage. This solution compensates for a change in ambient temperature; however, the specimen itself heats in this experiment. Therefore, a “dummy” gage would not suffice to compensate for temperature change.

A LabVIEW program, “Trigger Voltage Set.vi”, was created to counteract the temperature effects experienced by the strain gage. This program continually updated the reference voltage of the comparator to follow the strain gage’s drift. A user specified the maximum amplitude of the

signal in volts, the maximum amplitude in microstrain, and the desired strain level in microstrain (Fig. 3.5).

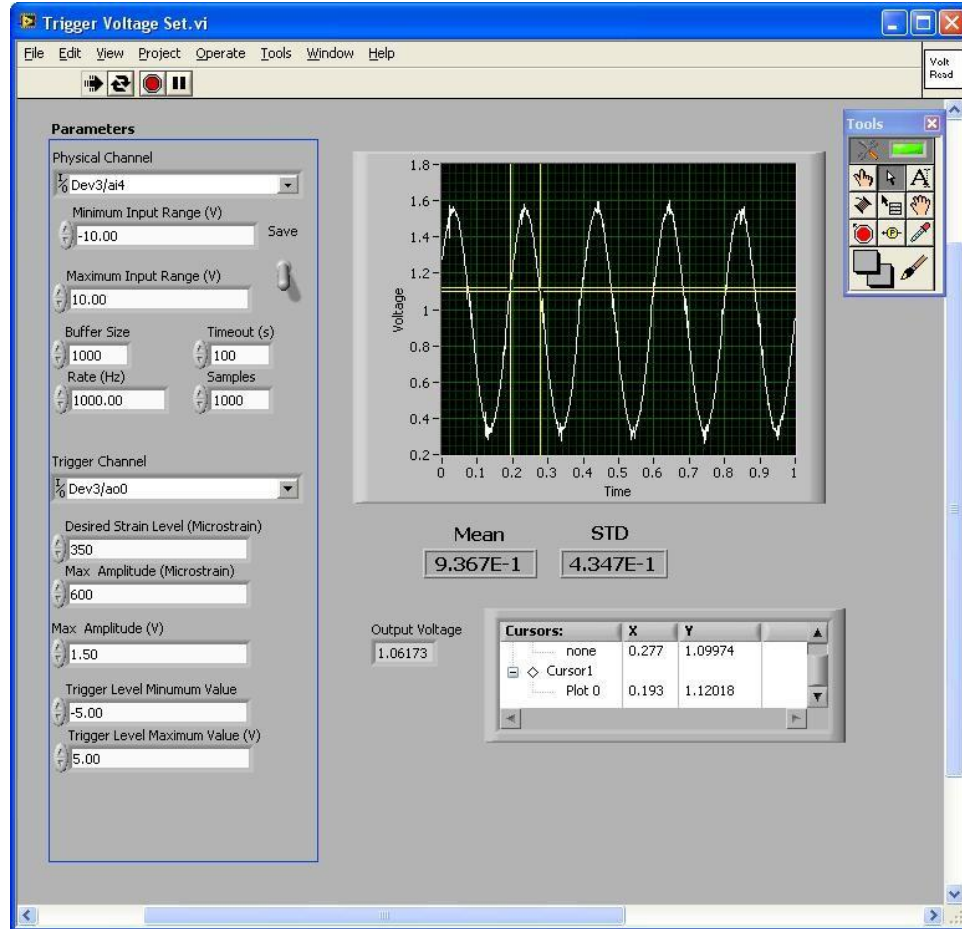


Fig. 3.5. Screenshot of LabVIEW program used to update reference voltage of the comparator.

The desired strain level divided by the maximum amplitude in microstrain provided a ratio to multiply the maximum voltage. The maximum voltage divided by two was then subtracted from this number and the average voltage was added. This determined the trigger voltage. Equation 3 represents this calculation,

$$V_{trigger} = \frac{\varepsilon_{desired}}{\varepsilon_{max}} V_{max} - \frac{V_{max}}{2} + V_{avg}. \quad (3.3)$$

The program read in the amplified strain gage signal, calculated the mean voltage, and determined the change in the mean voltage from the mean of the initial zeroed signal. The change in the mean voltage was then added to the trigger voltage that represented the voltage at the desired strain level.

As the signal passes through the comparator, it then enters a triggering network to send a voltage pulse to the lamp. The network uses a 555 timer chip in monostable mode. When in monostable mode, the trigger pulse must be shorter than the output pulse. For the case presented here, the comparator creates a square wave function in which to trigger for a certain width on either the rising or falling edge of the pulses. The output pulse (the signal to the lamp) should be smaller than the comparator signal and variable. To do this, a trigger network was added.

The trigger network has a diode that suppresses a spike in voltage at the rising edge of the comparator signal. The diode allows a spike to occur at the falling edge, keeping the lamp from being triggered on both the rising and falling edges. If a trigger at the rising edge is desired, the input to the comparator simply needs to be swapped with the threshold voltage. The following diagram shows the trigger network.

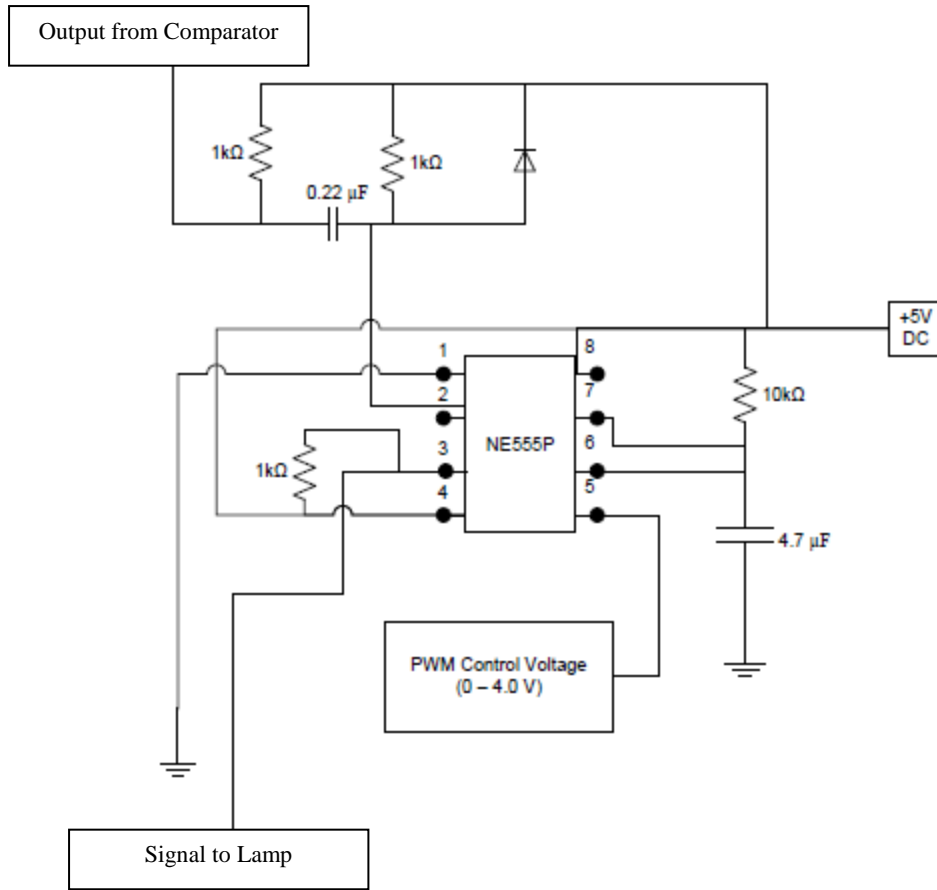


Fig. 3.6: Trigger network diagram

3.4 Theory of Operation

The strains of the specimen are assumed to be passed, in every respect, to the coating [7].

Theoretical Optical Strain Response involves five assumptions:

1. The specimen is in a state of plane stress, meaning:

$$\sigma_z = \tau_{xz} = \tau_{yz} = 0. \quad (3.4)$$

2. The strain on the specimen, ε^s , is transmitted to the coating, ε^c , without loss or amplification.

$$\varepsilon_x^s = \varepsilon_x^c, \quad (3.5a)$$

$$\varepsilon_y^s = \varepsilon_y^c, \quad (3.5b)$$

$$\varepsilon_z^s \neq \varepsilon_z^c. \quad (3.5c)$$

3. Plane stress also exists in the coating since it is relatively very thin.

$$\sigma_z^s = \sigma_z^c = 0. \quad (3.6)$$

4. The OSR in Eq. 5.7 can be thought of as a linear function since the coating coefficient, η , is much larger in comparison to the maximum shear strain, γ for low strain values.

$$OSR = \phi \frac{\frac{\gamma}{\eta}}{1 + \left(\frac{\gamma}{\eta}\right)^2} \approx \frac{\phi}{\eta} \gamma. \quad (3.7)$$

5. Excitation is modeled as parallel rays; the direction of excitation propagation to coating is the orientation of the LED lamp with respect to the specimen.

As the excitation passes through the coating, the polarization is changed due to the strain experienced by the specimen. This polarization change due to stress (or strain) is then captured in the intensity of the images. This intensity is related to the optical strain response that, when calibrated, indicates the strain field experienced by the specimen.

A CCD camera is used to capture the OSR. The intensity of the eight images captured of the specimen at various analyzer angles is compared to the average intensity of all the images spanning 180° to determine the amplitude and phase of the response. The LPC emission at a pixel is characterized by [12]:

$$\frac{I}{I_{avg}} = 1 + F \sin(2\alpha - 2G), \quad (3.8)$$

where I is the emission intensity at the given analyzer angle, α , and I_{avg} is the average intensity over all analyzer angles. This relationship can be seen clearly in Fig. 3.7.

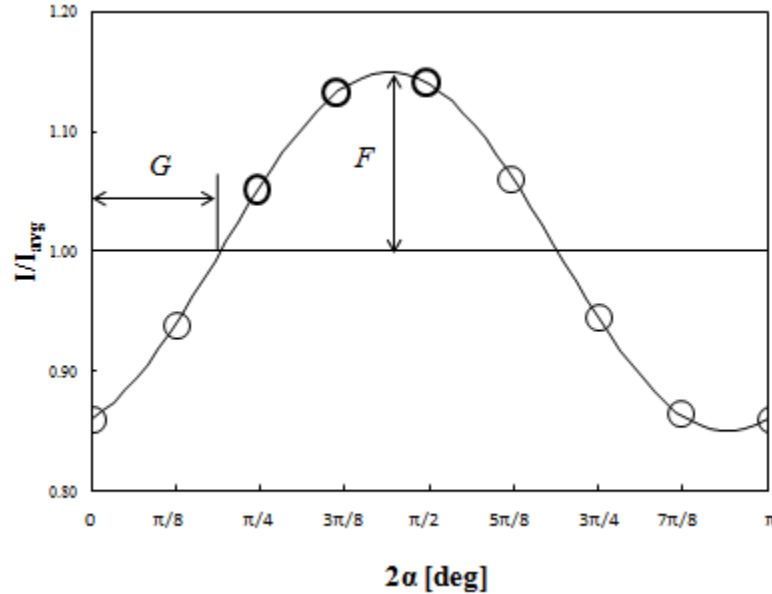


Fig. 3.7. Theoretical relationship between emission intensity and analyzer angle.

The amplitude, or magnitude of the OSR, F , is a function of the polarization efficiency and a calibration coefficient [12],

$$F = \phi \frac{\gamma}{1 + (\frac{\gamma}{\eta})^2}, \quad (3.9)$$

where ϕ is the polarization efficiency, γ is the in-plane maximum shear strain, and η is the coating coefficient. These parameters are characterized by the following relations:

$$\eta = \frac{a_b \lambda^*}{2 \pi K}, \quad (3.10)$$

and

$$\phi = f \left(\frac{I_{\perp}}{I_{\parallel}} \right). \quad (3.11)$$

The coating coefficient, η , is a function of the absorptivity, a_b , the effective wavelength, λ^* , and the optical sensitivity coefficient, K . The polarization efficiency, ϕ , is strongly correlated with the emission anisotropy of the coating and is often modeled as this value [13]:

$$r = \frac{1 - I_{\perp}/I_{\parallel}}{1 + 2 \left(\frac{I_{\perp}}{I_{\parallel}} \right)}. \quad (3.12)$$

Using the theoretical strain values and the fixed polarization efficiency, the calibration coefficient is determined using the regression to find the value minimizing the mean square error between theoretical and experimental results.

Preliminary tests were conducted to determine if the coating has a sufficient response time for up to 10 Hz loading. In this case, the CCD camera was replaced by a TAOS TSL-12S photosensor to monitor the time-dependent response of the coating in comparison to the strain gage. This photosensor acquired the emission intensity of a small area of the specimen while the excitation was held constant [12]. The time-dependent response of the coating and strain gage are shown in Fig. 3.8.

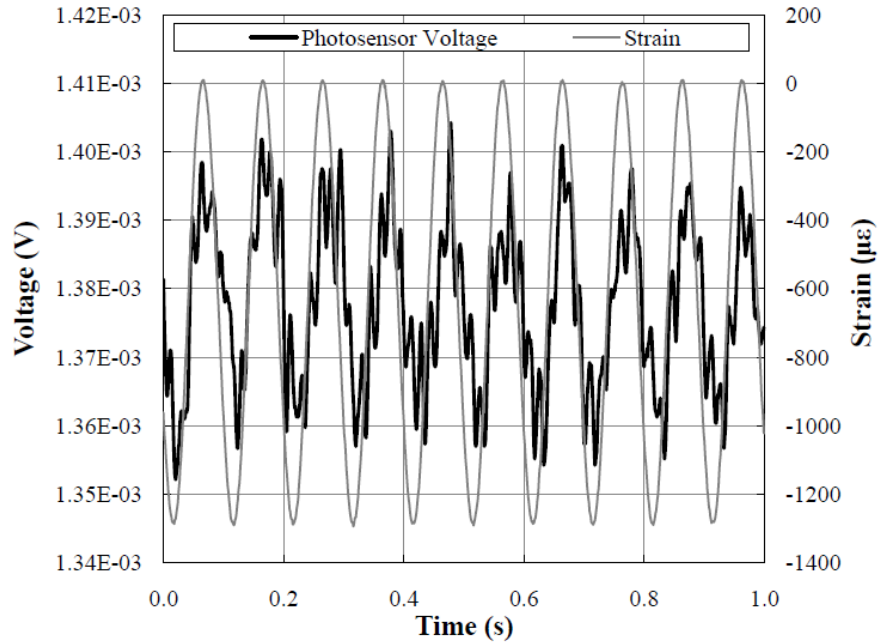


Fig. 3.8. Time-dependent photosensor (coating) and strain gage response during 10 Hz dynamic loading [12].

The coating was also tested for any loss in magnitude over a frequency range. The specimen was loaded between 2-10 Hz frequencies and the root-mean-square amplitudes of the photosensor and strain gage responses were acquired. Fig. 3.9 shows constant rms amplitude for the coating and strain gage responses. This indicates a consistent response with no loss in magnitude from the coating in this frequency range [12].

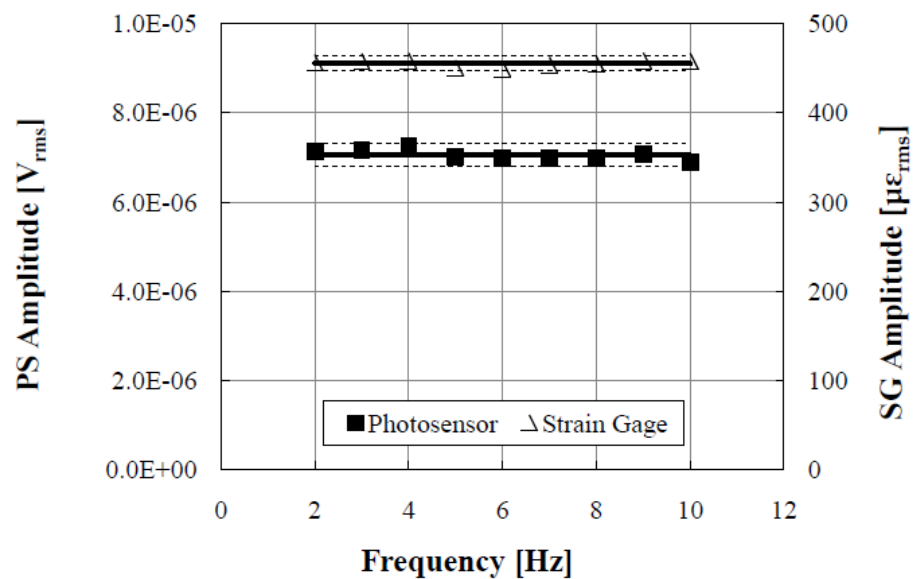


Fig. 3.9. Root-mean-square (rms) amplitude of the respective signals at the measured peak-frequency.

EXPLANATION OF LAB EQUIPMENT AND COATING PROCEDURE

4.1 Luminescent Imaging Lab

The Luminescent Imaging Lab is located in Hardaway Hall on the University of Alabama's campus. This research lab is where the experimental equipment was arranged and imaging experiments were conducted. The lab contains items such as: a CCD camera, 2D and 3D specimens, an LED lamp, optical posts, optical filters, an optical table, data acquisition devices, computers, a circuit breadboard, voltage generators, and a motor. The specific equipment used for this research is detailed in the following sections.

4.1.1 LED Lamp

The LED lamp used to excite the coating is an LM2X-DM LED light source made by Innovative Scientific Solutions, Inc. The 460 model has a published wavelength of light 458.2 nm with a bandwidth of 30.7 nm [14]. This wavelength was verified by Takahashi [2]. The two wavelength measures are seen in Fig. 4.1a and b.

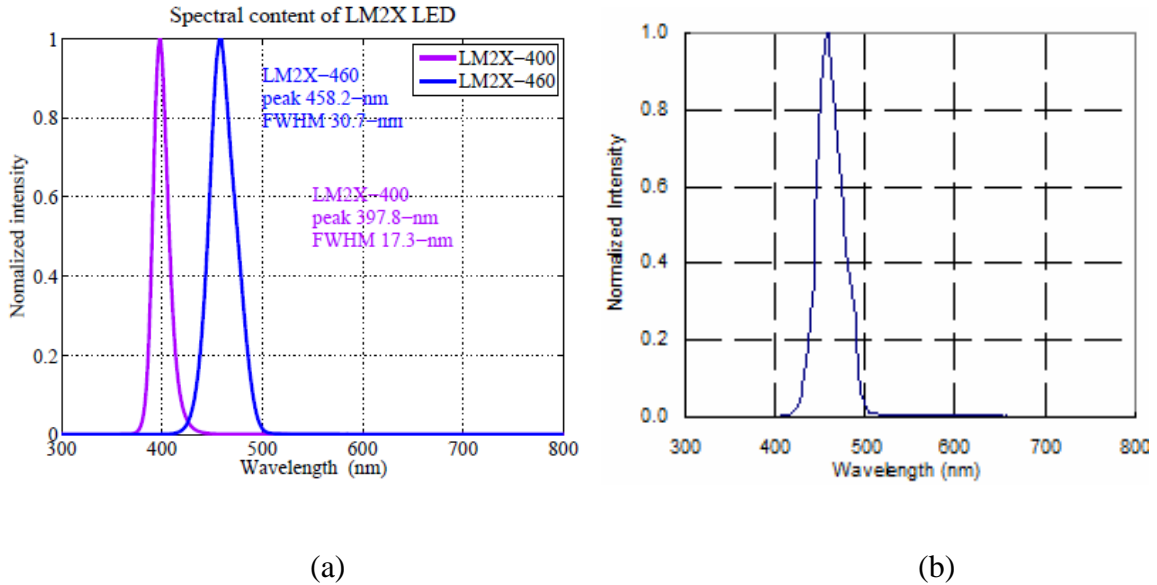


Fig. 4.1. (a) Published [14] spectral measurement and (b) measured spectral emission of LEM2X-DM [2].

This experiment used both operating modes of the lamp, continuous and pulse, which were changed via an external toggle switch on the lamp. Continuous mode required a constant power supply to obtain the necessary voltage. Pulse mode required a voltage trigger signal through a BNC cable. The signal used was a square wave ranging from 0 V to 5 V, flashing the lamp on and off. This signal was sent from the circuit and enabled the lamp to pulse on for a specific length of time. The lamp has a published rise time (10%-90%) of less than 5- μ s and a fall time (90%-10%) of less than 250 μ s. The manufacturer's trigger signal and the LEM2X-DM response is shown in Fig. 4.2 [14].

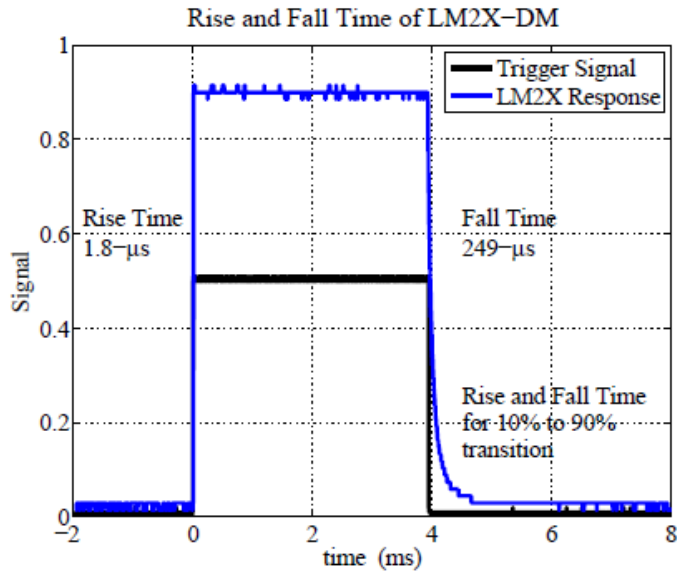


Fig. 4.2. Published plot of a 4-ms trigger signal and the LEM2X-DM response [14].

4.1.2 CCD Camera

Roper Scientific's PIXIS: 1024B is a back-illuminated CCD camera that is used for quantitative scientific imaging. Back illumination provides the highest sensitivity available for the visible region of light. The camera also features a 1024x1024 imaging array providing high spatial resolution. The scientific grade of the camera offers low noise, few defects, and a linear response. The specimen coating emits orange light when excited, a wavelength of approximately 600 nm. A Nikon 50mm f/1.2 lens is attached to the camera to manually focus the images. At this wavelength, the quantum efficiency of the PIXIS: 1024B is close to 95% (Fig. 4.3) [15].

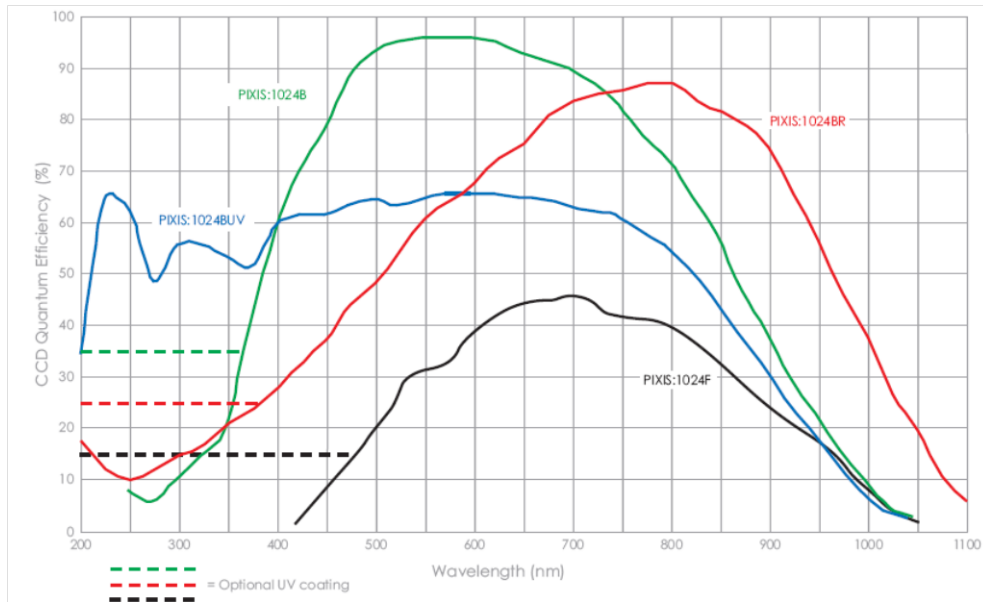


Fig. 4.3. Quantum Efficiency of different PIXIS 1024 CCD cameras [15].

4.1.3 Analyzer Rotation Stage

Newport Corporation's ESP 300 Motion Controller/Driver was used to control their URC-100CC rotation stage. This stage rotates the analyzer placed in front of the CCD camera. The stage was rotated from 0° to 157.5° at intervals for 22.5° . The accuracy of the rotation stage is 0.03° [2]. Fig. 4.4 shows the LED lamp, CCD camera, and the rotation stage on an optical post.

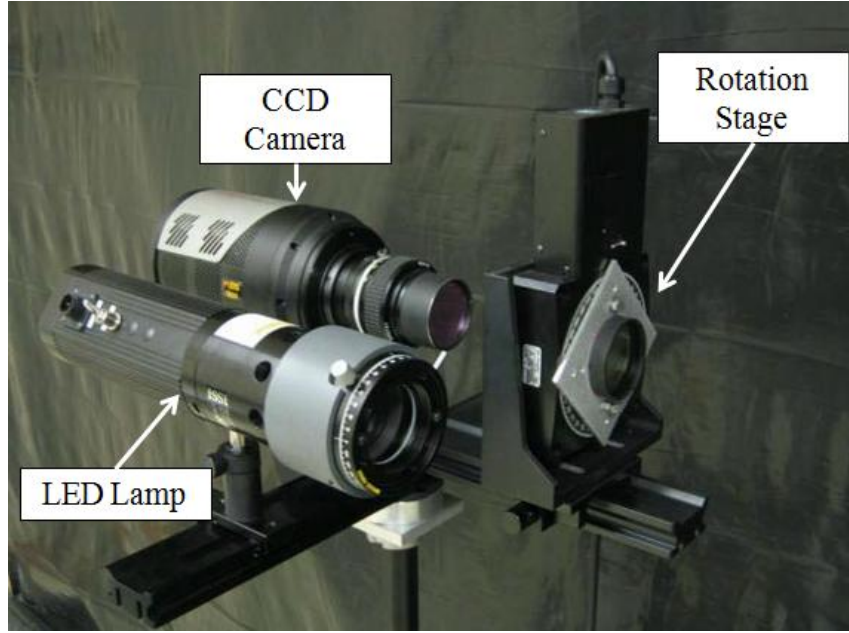


Fig. 4.4. Image of the excitation source imaging setup.

4.1.4 Optics

For this imaging setup, two dichroic polarizers, one achromatic quarter-wave plates, and one bandpass interference filter were used. The two polarizers allow for wavelengths between 380 and 780 nm. This is compatible for both the 465 nm excitation and the 600 nm emission wavelength. These polarizers allow 30% of the light to pass through [2]. The first polarizer and quarter-wave plate were located in front of the excitation source. Once the excitation passes through this polarizer, it passes through a quarter-wave plate with a retarder accuracy of $\pm\lambda/100$ [16]. This sequence of optics (linear polarizer followed by quarter-wave plate) creates circularly polarized light that will excite the coating.

The emitting light (luminescence) first passes through the second linear polarizer and a bandpass interference filter. This filter is a 600 nm bandpass filter (40 nm full-width-half maximum) manufactured by Melles Griot. Fig. 4.5 shows the emission spectrum for the luminescent

coating. There are two peaks between 550 nm and 600 nm. The 600 nm filter is preferred over the 500, 550, and 650 nm filters as it rejects the most excitation relative to capturing the most emission [2].

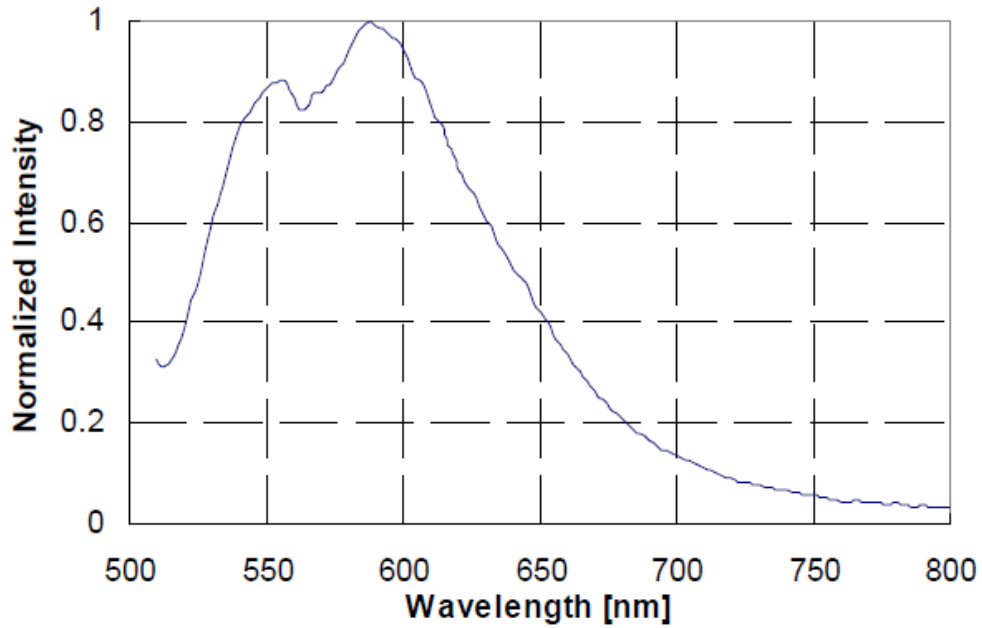


Fig. 4.5. Emission spectrum of luminescent photoelastic coating [2].

4.1.5 Motor and Variable Drive

The drive used to control the motor is an AutomationDirect GS2-11P0 AC Drive. The drive has a single-phase input (100-120 VAC) and three-phase output (200-240 VAC). The rated output frequency ranges from 1.0 to 400 Hz with a resolution of 0.1 Hz. An in-house LabVIEW program, “motor_run2.vi”, created a user interface for controlling the motor. The motor is connected to the computer through an RS-232 Modbus port on the COM1 port and the program communicates to the motor through the MODBUS serial protocol [17]. The motor used to deflect the specimens was a Marathon Electric three phase inverter duty AC induction motor. The motor operates at 230V with a maximum RPM of 5400.

4.1.6 Timing Circuit Components

The circuit was created on a 3M solderless breadboard. The instrumentation amplifier and comparator consist of LM741 op amps manufactured by Texas Instruments. This op amp has a maximum rated supply voltage of ± 22 V, a maximum rated input voltage of ± 15 V, and a maximum rated differential input voltage of ± 30 V. The operating temperature is between -55 °C to +125 °C [18].

The reference voltage for the comparator is determined by a LabVIEW program, “Trigger Voltage Set.vi”. The output signal from the instrumentation amplifier is read through a National Instruments SCC-68 I/O connector block. Wires are connected to analog input screw terminals and read into “Trigger Voltage Set.vi”. The program analyzes this signal and determines an output voltage that is sent out through analog output screw terminals. This analog output is used as the reference voltage for the comparator.

The NE555 precision timing chip from Texas Instruments is used to create the pulse-width modulation. This chip can operate in astable or monostable mode. The monostable mode is used for this application. In this mode, the output goes high when the input goes low. The maximum rated supply voltage and input voltage for the chip is 18 V [19].

4.1.7 Oscilloscope

A Rigol DS1052E oscilloscope was used to view the various signals in the circuit. This oscilloscope has two analog channels and an external trigger. When using one or two channels, the sample rate is 1 GSa/s and 500 MSa/s, respectively. An image of the oscilloscope displaying a signal is shown in the Fig. below (Fig. 4.6).

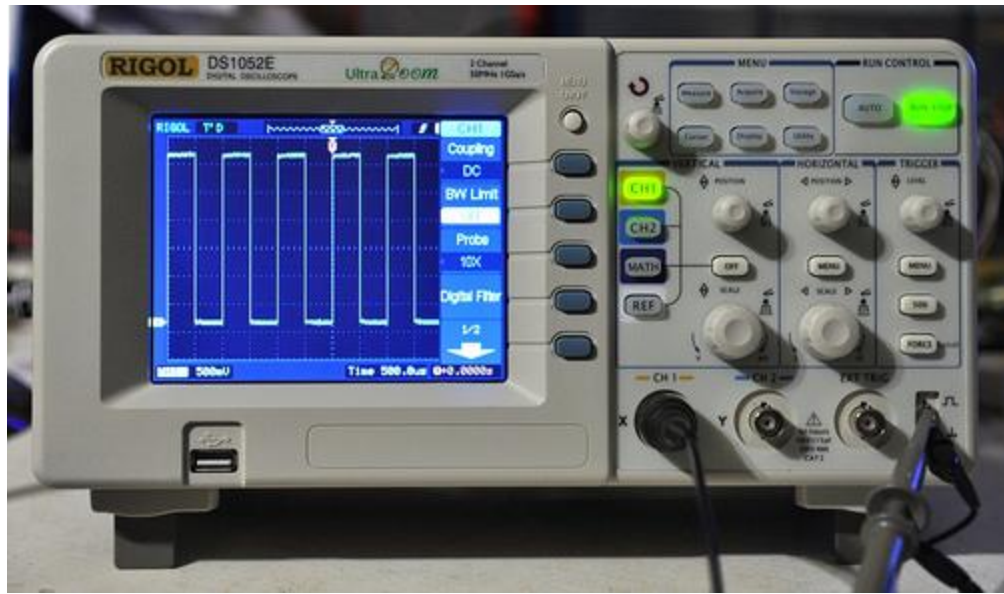


Fig. 4.6. Image of Rigol DS1052E Digital Oscilloscope.

4.1.8 Voltage Generators

Two voltage generators are used for the circuit. One is used as the supply voltage for the comparator, and the other is used as the pulse-width modulation voltage (determining the length of the pulse). They are both the BK1621A model made by B&K Precision. The generators can output anywhere from 0-18 VDC with 0-5A of current output. This model has a $.02\% \pm 3 \text{ mV}$ load regulation and a 2% LED voltmeter accuracy [21].

4.1.9 Bending Apparatus

The apparatus used to clamp one end of the specimen was designed by Gerber [12]. The reaction beam is a square tube measuring 7.62 x 7.62 x 45.72 cm with 0.635 cm thickness. Steel L-brackets fasten the reaction beam to an optical table. An aluminum clamp is attached at the top of the reaction beam. This clamp secures the specimen in a vertical orientation. The motor is placed in front of the specimen so that the cam is aligned to be resting against the specimen without deflecting it. Fig. 4.7 shows the apparatus with a specimen in place.

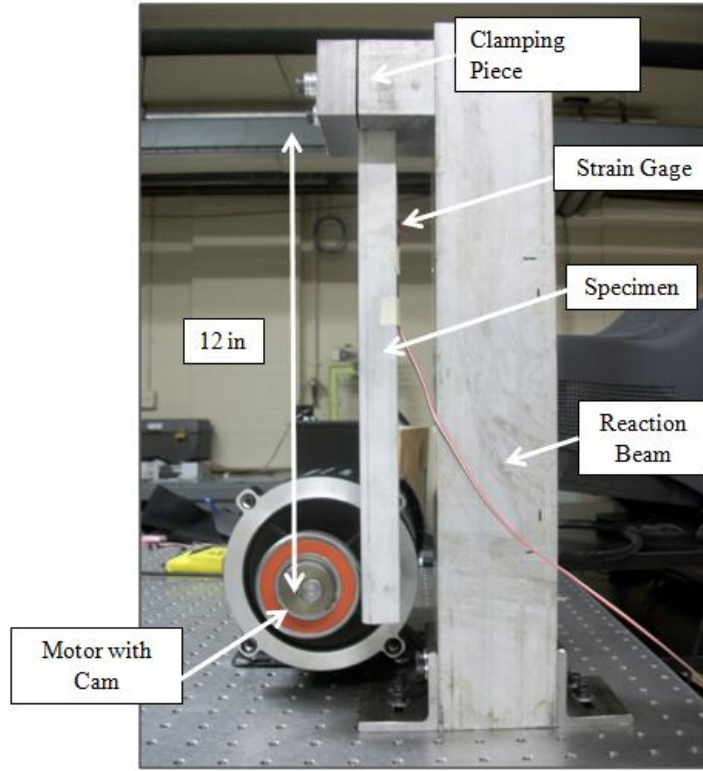


Fig. 4.7. Reaction beam used to clamp one end of a specimen.

4.1.10 Software

Most of the software used was developed in LabVIEW by students working in the lab. A brief description of the various software programs is provided here:

“motor run 2.vi”, created to control the variable drive and communicated via a modbus port to the driver. The options include: run or stop the motor, forward or reverse direction, and frequency input. The additional inputs are used to communicate to the proper addresses and were left to default once determined. Fig. 4.8 is a screenshot of the program.

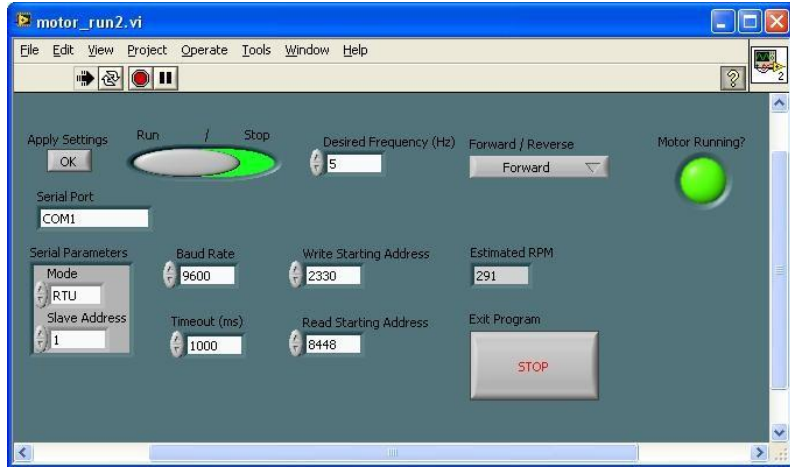


Fig. 4.8. Screenshot of LabVIEW program used to control variable drive.

“Trigger Voltage Set.vi”, used to calculate the trigger (or reference) voltage for the comparator.

This program was discussed in detail in section 3.3.3. The options of this program include:

minimum and maximum input voltage range and trigger voltage, buffer size, timeout, number of samples, rate of sampling, maximum amplitude in voltage and in microstrain, and the desired trigger strain level. To reiterate, the program follows the strain gage drift due to temperature effects and constantly updates the reference voltage for the comparator. An image of the program is shown in Fig. 4.9.

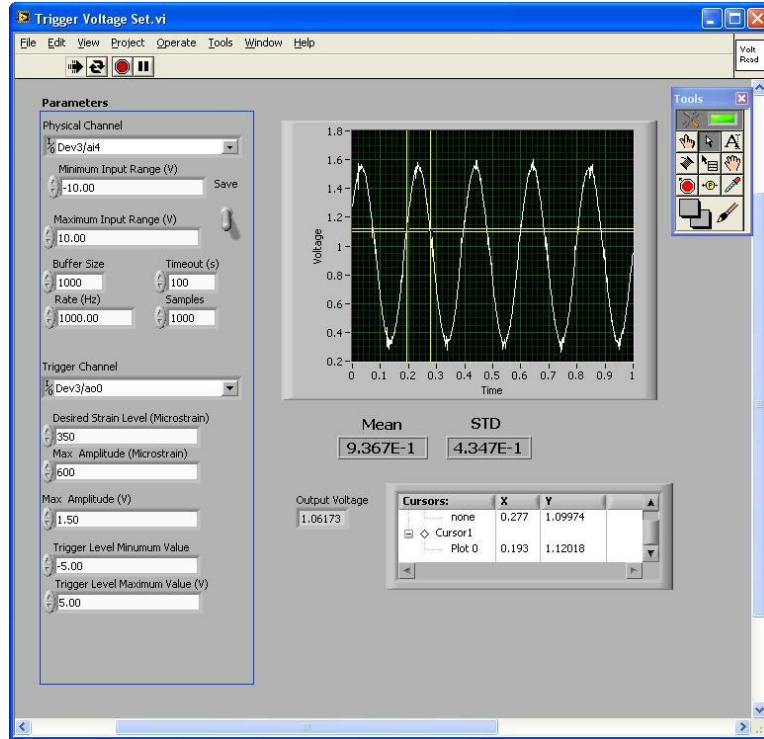


Fig. 4.9. Screenshot of LabVIEW program used to update the reference voltage for the comparator.

“LPC Acquisition.vi” used to acquire the image sequence of the unloaded and loaded specimen. The program allows the user to input an exposure time for a single image or a sequence of images, choose a region of interest, attain and save a sequence of images, set the analyzer position, choose the analyzer angles to use when acquiring a sequence of images, view an image, and check the intensity value at any point in the image. When a sequence of images is acquired, the load state and analyzer angle of each image is contained in the file name to facilitate file reading in the analysis stage. Additional parameters include choosing which LED lamp was going to be used and which camera was going to be used. These features were not used in this experiment as the LED lamp was controlled separately and only one camera was used. Fig. 4.10 shows a view of the program.

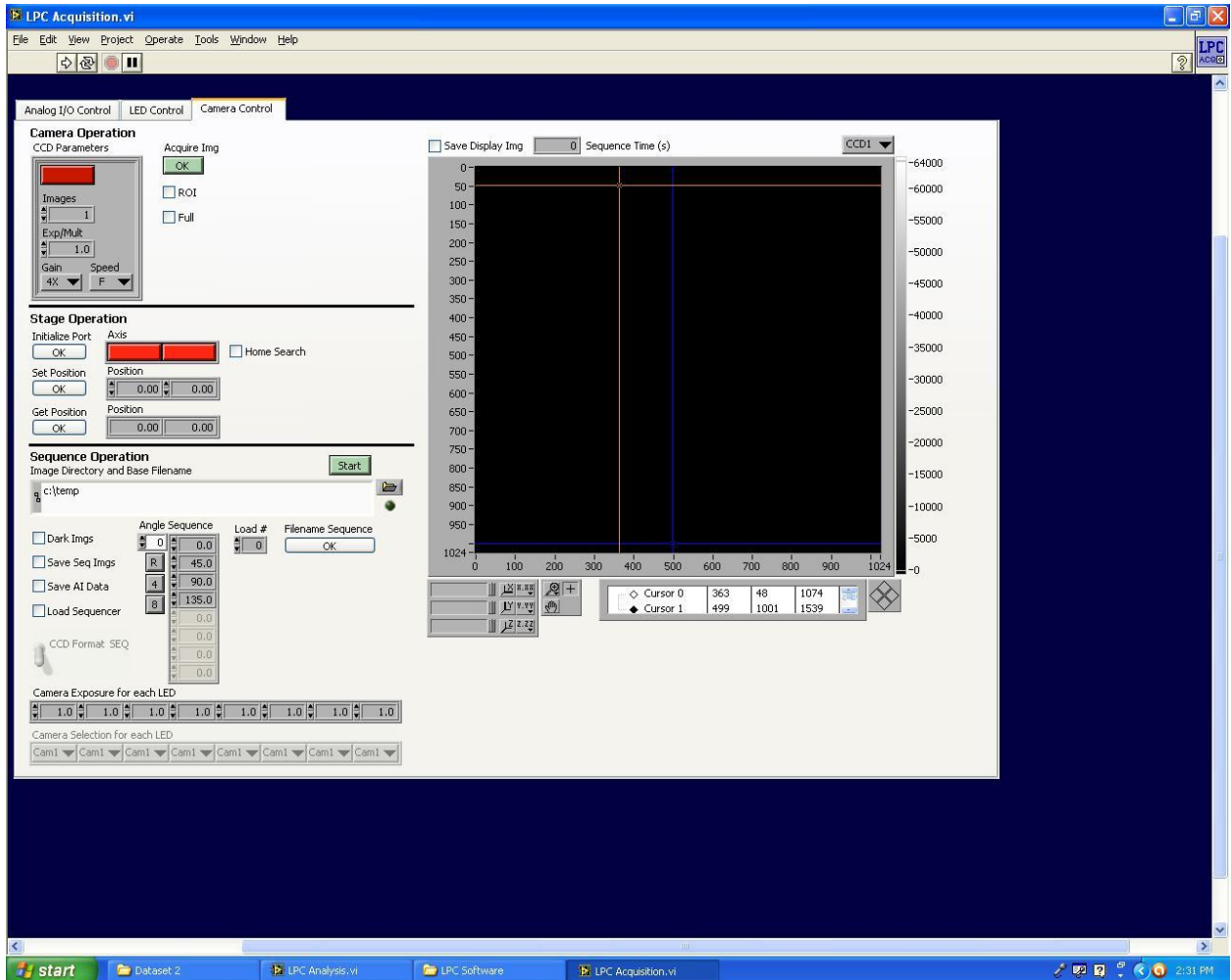


Fig. 4.10. Screenshot of program used to acquire images.

“LPC Analysis.vi”, used to analyze the images once all have been acquired. When a sequence of images is acquired, the first step is to read in all of the loaded images in Image Processing mode. An option, called “chk,” checks the images for a sinusoidal intensity response. A crosshair is placed at a point on the top image and then dragged vertically along the image. This crosshair selects a pixel to plot the intensity for each image of the analyzer sequence. The intensity is relative to the average intensity of all images over 180° . Fig. 4.11 shows an image of the program.

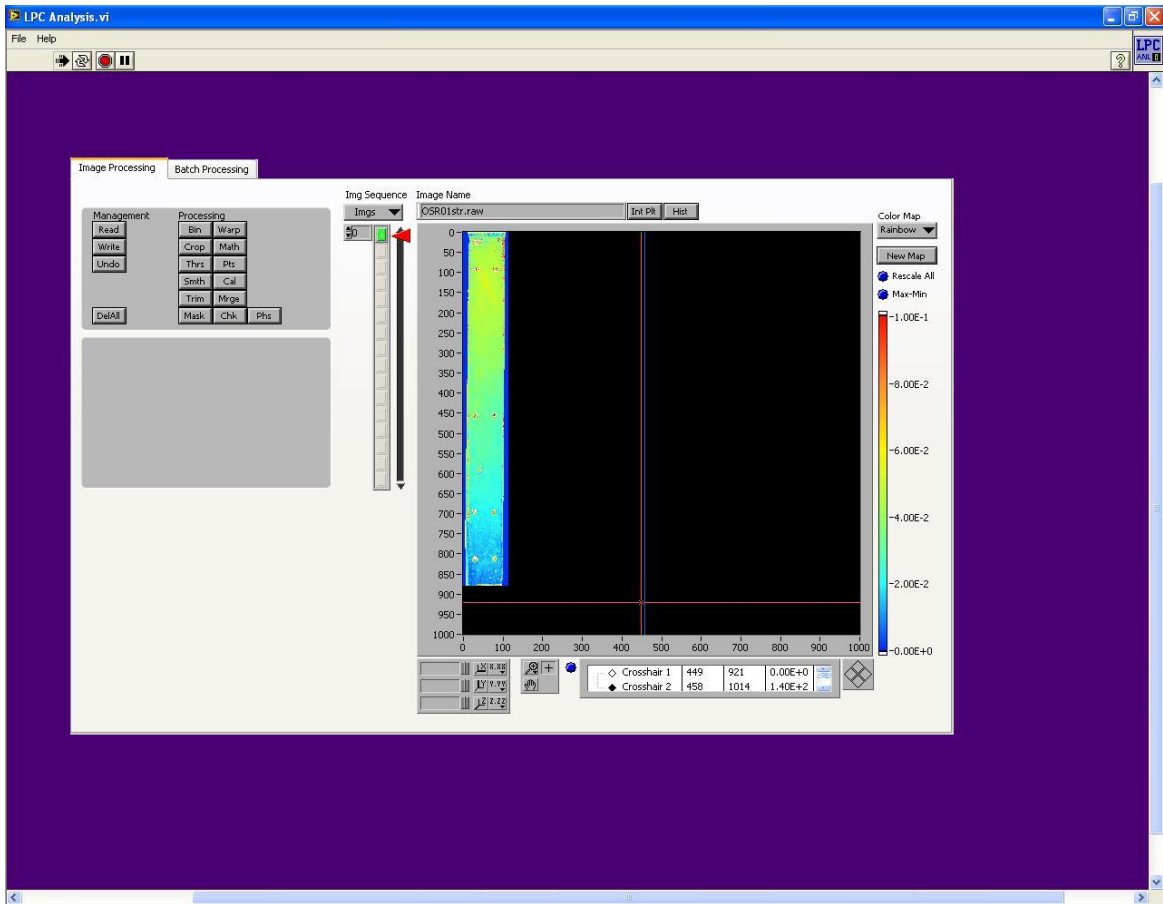


Fig. 4.11. Screenshot of program used to analyze images.

Once the response is validated, a reference image, loaded image, and dark image are read in. The program subtracts any residual intensity captured in the dark image from both the reference and loaded images. The corrected unloaded image is shown in the program's viewing window. The next step is to use the “pts” option to locate the target points on the specimen. Each specimen was marked with eight target points on each side. The coordinates of these points are saved in a text file for later use.

An analysis of the data can begin after the target file has been generated. In the Batch Mode, an initial file is chosen for each load state as well as a target file. The program then reads in sequential images based on the user indicated analyzer angles and load states. The program

assesses the translation of the target points from each state using a rigid body translation fit to ensure the proper pixel of the corresponding unloaded image is compared to the pixel on the loaded image. The images are compared assuming rigid body translation. The analysis provides two OSR images and two phase images for each analyzed set of data. Optical Strain Response data is determined from the OSR image corresponding with the loaded state, as is phase data.

4.1.11 Specimens

All specimens were aluminum 6061-T6 with a Young's modulus of 70 GPa and a Poisson's ratio of 0.33. The tube specimens measured 2.54 x 2.54 x 30.5 cm with a thickness of 0.37 cm. The dimension from the point of application of the load to the clamped end is 30.5 cm. The tube specimens were sprayed on three sides, leaving the backside available for the strain gage. The bar specimen measured 2.54 x 21.6 cm with a thickness of 0.67 cm. The bar specimen was sprayed with coating on the front (tensile) side. Strain gages were applied to the back of all specimens about 6.35 cm from the clamped end. The imaged sides were marked with target points used for image registration during the analysis process.



Fig. 4.12. Coated specimens.

4.2 Coating Preparation Lab

This lab is located in room 224 of the AIME Building on campus. It is used as a space to mix and apply the coating to the specimens. When applying the coating, a fume hood is used to ventilate the environment from potentially harmful fumes. The coating is applied with an airbrush inside the fume hood and periodically set to cure by UV light.

4.2.1 Balances

Two balances are used for measuring the materials of the coating. A balance manufactured by Denver Instrument Company is used for its high resolution; meanwhile a balance manufactured by Adam Equipment (CQT 1501) is used for its high range. The Denver Instrument Company balance can hold up to 150 g at 0.001 g resolution, and the Adam Equipment balance holds up to 1500 g at 0.01 g resolution. The higher capacity of the Adam Equipment balance is useful when a large batch of the coating is produced. The high resolution is necessary for accurate measurements of the less abundant materials, particularly the dyes.

4.2.2 Coating Thickness Instrument

A contact-eddy probe manufactured by DeFelsko Corporation is used to measure the thickness of the coating applied to metallic specimens and once completely cured. The probe can measure up to 0.1 μm resolution as well as calculate the mean, standard deviation, maximum, and minimum for a series of readings.

4.2.3 Fume Hood

An Air Sentry high performance fume hood is used during the coating process. This fume hood operates at 70-80 linear feet per minute and pressurized air from the fume hood is used for the airbrush. Fig. 4.13 is an image of the type of fume hood used.



Fig. 4.13. Air Sentry high performance fume hood.

4.2.4 UV Lamps

A Spectroline high-intensity ultraviolet lamp is used to cure the specimens. The particular lamp used is a model SB-100P that emits light at a wavelength of 365nm and an intensity of 4800 $\mu\text{W}/\text{cm}^2$ at 15 inches. The lamp requires 120 volts for power and operates at a frequency of 60 Hz [22]. Depending on how large the surface area that needs curing, more than one of these lamps is used at a time. Fig. 4.14 shows one of these UV lamps.



Fig. 4.14. High-intensity ultraviolet light used to cure the specimens.

4.3 Coating Technique

With the exception of the luminescent and absorption dyes, the chemicals used in the coating are all measured and left to mix overnight in a glass beaker using a magnetic stirrer. The next day, the absorption and luminescent dyes are added to the mix and the solution is left to stir for an additional few hours. The amount of coating needed to reach the nominal thickness of 400 μm is estimated in an Excel spreadsheet using a set formula by weight. The calculation accounts for overspray: 40% on the 2D specimens where only one side is coated and 60% on the 3D specimens where two sides are coated. As the coating is stirring, the airbrush, fume hood, and specimens are prepared.

The airbrush is a conventional aerosol sprayer made by Paasche, model H [23]. It is connected to the compressed air and the pressure is held nearly constant at about 20 psi. Newspaper is taped on the walls of the fume hood to keep from spraying the coating on the fume hood itself.

Prior to coating the specimens, they are lightly sanded and rinsed with acetone to clean the surfaces. Tape is then applied on each end of the specimens to designate an area at least 15 cm and 20 cm long on the 2D and 3D specimens, respectively. Once ready, the specimen is coated with a 3 mL batch of coating for the first layer. Then the specimen is set outside of the fume hood to cure underneath the UV lamps for about 15-20 minutes. After this short cure time, the specimen is coated in 5 mL batches with a 15-10 minute cure time between layers. The cure time between layers ensures the coating cures all the way through. Once all of the coating has been applied, the specimen is set aside for a final cure time of about 6 hours. According to previous research done by Gerber [13], a 6 hour cure time is appropriate.

STRAIN SEPARATION RESULTS AND DISCUSSION

For dynamic measurements, images of the specimen of interest were produced by strobing a light source in synchronization with the motion of the specimen. The camera's shutter was left open for an extended period of time until acceptable image intensity was reached. An LED lamp was used for the light source along with a charge-coupled device camera for the imaging. A cam was attached to an electric motor with variable frequency. The cam was initially placed lightly against the specimen when the beam was not deflected. The cam deflected the specimen in a harmonic motion when the motor was activated.

The specimens were loaded as cantilever beams: clamped on one end and loaded on the free end (Fig. 5.1). The 2D bar specimen was imaged on the tension side, while the 3D tube specimens were imaged on both the tension and neutral-axis faces. Parallel and oblique ($\psi = 55^\circ$) sets of images were acquired for each imaged side of the specimens. The 55° oblique incidence angle was chosen as it showed the optimum SNR between the image intensity (signal) and photonic shot noise of the CCD camera (noise) [2]. Using both of these sets of images, strain separation was performed to determine the experimental principal strains. The experimental OSR was compared to the theoretical OSR to assess the accuracy of the results.

5.1 Image Acquisition and Processing

Tests were conducted in the Luminescent Imaging Lab. The specimens were mounted as described in section 4.1.9. The CCD camera and LED light were mounted on a tripod

across from the specimen, with the camera aligned and focused to capture the specimen image.

Images were acquired in complete darkness with the exception of the excitation lamp.

Prior to acquiring images, an anisotropy test was performed on the unloaded specimen to determine the calibration coefficients discussed earlier. This test involved removing the linear polarizer and quarter-wave plate off of the LED lamp and replacing it with a linear polarizer. One image was acquired with this linear polarizer parallel to the analyzer and another was acquired perpendicular to the analyzer. In analysis, the perpendicular image was divided by the parallel image, I_{\perp}/I_{\parallel} , and the average value of intensity was recorded and entered in the equation for anisotropy (3.12). This anisotropy value was modeled as the value for the polarization efficiency.

The LabVIEW program, “LPC Acquisition.vi”, was used to acquire images of the unloaded and loaded specimen. Exposure time for the loaded images was around 540-600 s, depending on the pulse-width of the voltage signal sent to the lamp and the frequency of the motor. The lens f/stop was set to 1.2. Loaded and unloaded images were acquired for each load state. The unloaded images were acquired with the motor off and the cam in the undeflected position. For the unloaded images, the LED lamp was left in DC mode to continuously illuminate the specimen. Rather than a 540-600 s exposure time, these images needed just 13 s to obtain the similar intensity. A dark-field image was also obtained for each load state to correct for any residual voltage in the camera pixels. This image was subtracted off from each image to produce corrected images.

5.2 Theoretical Modeling

The applied load was modeled as a point load, and linear beam theory was used to estimate the deflection and strain. Theoretical OSR was determined using theoretical equations for LPC. These equations required determining two calibration coefficients that are unique to each coated specimen.

The LPC Analysis software enables the user to output OSR relative to pixel number (location). The pixel numbers were converted to spatial distances using known distances of targets points placed on the specimen and the corresponding pixel numbers from the image. A simple line equation was developed to calculate the distance from the point of application (POA) of the load to the given pixel, $P(P_{xi}, P_{yi})$,

$$x = (P_{y1} - P_{yi}) * \frac{d_2}{P_{y1} - P_{y2}} + d_1. \quad (5.1)$$

Fig. 5.1 clarifies the coordinate system and the definition of the variables used in (5.1).

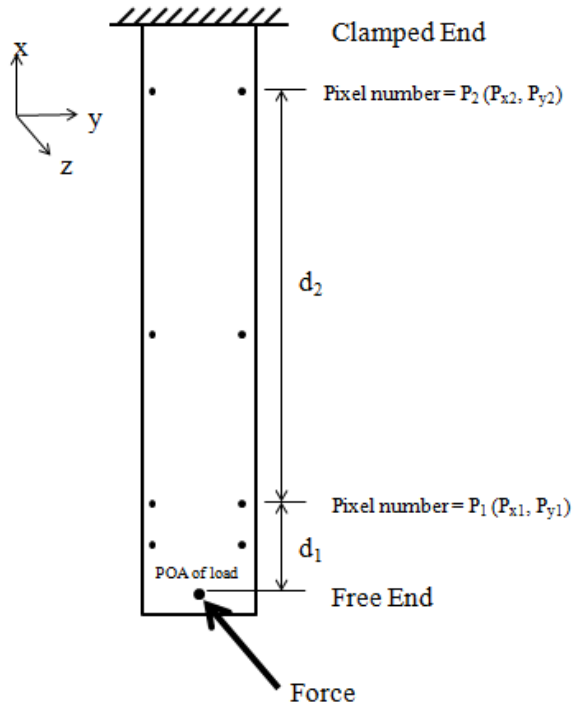


Fig. 5.1. Diagram showing variable definitions to convert pixels to inches.

Once the target point locations were determined, the theoretical stress in the x-direction (a known principal stress direction) was calculated using beam dimensions and properties:

$$\sigma_x = \frac{3E\delta_d t_s x}{2L^3}, \quad (5.2)$$

where E is the Young's Modulus of aluminum, δ_d is the deflection of the beam, t_s is the thickness of specimen, x is the distance from the point of application of the load, and L is the length from the point of application of the load to the clamped end. Hooke's Law was then used to determine the strain in both the x and y directions:

$$\varepsilon_x = \frac{\sigma_x}{E}, \quad (5.3)$$

$$\varepsilon_y = -\nu\varepsilon_x = \frac{-\nu\sigma_x}{E}. \quad (5.4)$$

For parallel excitation in which the propagation of the excitation and emission travels through a plane nearly perpendicular to the surface, the theoretical maximum in-plane shear strain is the difference between the principal strains in the x and y directions,

$$\gamma_{max,p} = \varepsilon_x - \varepsilon_y. \quad (5.5)$$

The principal strains will be designated with subscripts 1 and 2, thus

$$\varepsilon_x = \varepsilon_1, \quad (5.6a)$$

$$\varepsilon_y = \varepsilon_2. \quad (5.6b)$$

The equation becomes more complicated for oblique excitation. Because the excitation travels in a plane that is no longer parallel to the surface, the strain in the z-direction can no longer be neglected. This is a principal strain as well ($\varepsilon_z = \varepsilon_3$). The excitation is rotated about the x-axis by the angle ψ . The incidence angle within the coating is ψ' , and this is calculated using Snell's Law that relates the sines of the angles of incidence to the index of refraction of air, $n_a = 1$, and the coating, n_c ,

$$\frac{\sin \psi}{\sin \psi'} = \frac{n_c}{n_a}. \quad (5.7)$$

Due to refraction effects, the oblique incidence angle within the coating is ψ' , as shown in Fig.

5.2.

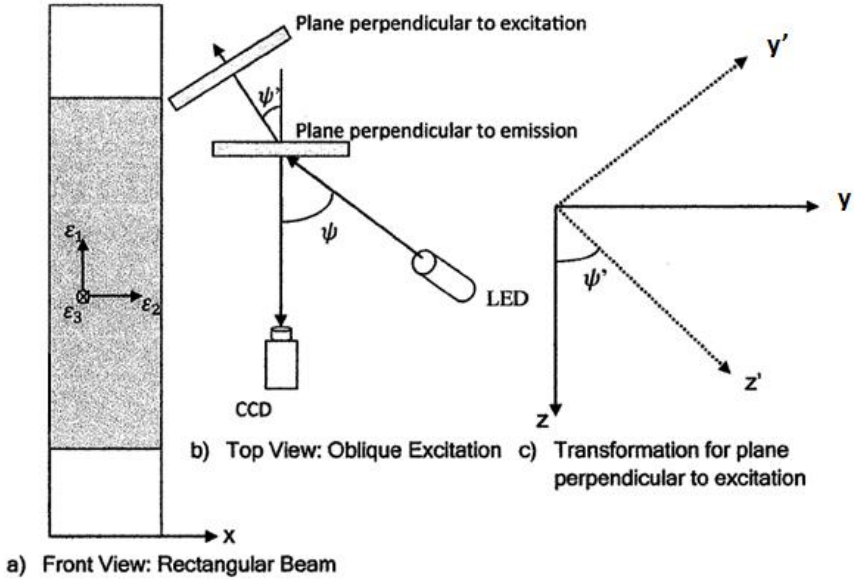


Fig. 5.2. Diagram showing oblique excitation and the plane rotation.

As a result of the rotation of the excitation about the principal axis, the z -component of strain will affect the OSR. The transformed strain becomes,

$$\varepsilon'_x = \varepsilon_1, \quad (5.8a)$$

$$\varepsilon'_y = \varepsilon_2 \cos^2 \psi' + \varepsilon_3 \sin^2 \psi' - \gamma_{yz} \sin \psi' \cos \psi', \quad (5.8b)$$

where γ_{yz} represents the shear strain in the yz -plane. Because z is a principal strain direction, $\gamma_{yz} = 0$. The out-of-plane normal strain, ε_3 , can be expressed in terms of the in-plane principal strains and the Poisson's ratio of the coating. Because the coating is under a plane state of stress, the out-of-plane component in terms of in-plane strains is:

$$\varepsilon_3 = \frac{\nu_c}{\nu_c - 1} (\varepsilon_1 + \varepsilon_2). \quad (5.9)$$

The rotated shear strain equation is:

$$\gamma_{max,o} = \varepsilon'_x - \varepsilon'_y. \quad (5.10)$$

Substituting equations (5.8) and (5.9) into (5.10) yields:

$$\gamma_{max,o} = \varepsilon_1 \left[1 - \left(\frac{\nu_c}{\nu_c - 1} \sin^2 \psi' \right) \right] - \varepsilon_2 \left[\cos^2 \psi' + \left(\frac{\nu_c}{\nu_c - 1} \sin^2 \psi' \right) \right]. \quad (5.11)$$

Thus, the OSR is a function of in-plane normal strains, out-of-plane normal strain, shear strain, effective excitation and emission wavelengths, Poisson's ratio and index of refraction of the coating, angle of incidence, as well as the calibration coefficients:

$$OSR = f(\varepsilon_x, \varepsilon_y, \varepsilon_z, \gamma_{xy}, \tilde{\lambda}_{ex}, \tilde{\lambda}_{em}, \nu_c, n_c, \psi', \phi, \eta). \quad (5.12)$$

The OSR for an image is now written in terms of the transformed shear strain [3],

$$OSR = \phi \frac{\gamma_{eff}/\eta}{1 + (\gamma_{eff}/\eta)^2}, \quad (5.13)$$

where the effective maximum in-plane shear strain is dependent on the transformed shear strain on the plane perpendicular to excitation and emission [3],

$$\gamma_{eff} = \frac{\gamma_{ex}}{\tilde{\lambda}_{ex}} + \frac{\gamma_{em}}{\tilde{\lambda}_{em}} \frac{\cos \psi'_{ex}}{\cos \psi'_{em}}. \quad (5.14)$$

Equation (5.14) is for parallel and oblique excitation, but can be reduced for each case. The term,

$\frac{\cos \psi'_{ex}}{\cos \psi'_{em}}$, corrects the retardation depth differences between the two cases. For parallel incidence,

$\gamma_{ex} = \gamma_{em} = \gamma_{max,p}$, and since $\psi'_{ex,p} = \psi'_{em}$, the term $\frac{\cos \psi'_{ex}}{\cos \psi'_{em,p}} = 1$, meaning the penetration

depths are the same. This causes equation (5.14) to reduce down to,

$$\gamma_{eff,p} = \gamma_{max,p}. \quad (5.15)$$

For oblique incidence, the same simplifications cannot be made. For this case, $\gamma_{ex} = \gamma_{max,o}$,

$\gamma_{em} = \gamma_{max,p}$, and $\frac{\cos\psi'_{ex}}{\cos\psi'_{em,o}} \neq 1$, because the penetration depths for excitation and emission are

different. This causes the maximum effective in-plane shear strain for oblique excitation to become:

$$\gamma_{eff,o} = \frac{\gamma_{max,o}}{\tilde{\lambda}_{ex}} + \frac{\gamma_{max,p}}{\tilde{\lambda}_{em}} \frac{\cos\psi'_{ex,o}}{\cos\psi'_{em}}. \quad (5.16)$$

By making the necessary substitutions for maximum in-plane shear strain for oblique and parallel excitation, the equation can be rewritten as:

$$\gamma_{eff,o} = \frac{\varepsilon'_x - \varepsilon'_y}{\tilde{\lambda}_{ex}} + \frac{\varepsilon_x - \varepsilon_y}{\tilde{\lambda}_{em}} \frac{\cos\psi'_{ex,o}}{\cos\psi'_{em}}. \quad (5.17)$$

Finally, in terms of principal strains,

$$\gamma_{eff,o} = \varepsilon_1 \left[\frac{1}{\tilde{\lambda}_{ex}} - \frac{\nu_c}{\nu_c-1} \frac{\sin^2\psi'}{\tilde{\lambda}_{ex}} + \frac{\cos\psi'_{ex}}{\tilde{\lambda}_{em}} \right] - \varepsilon_2 \left[\frac{\cos^2\psi'}{\tilde{\lambda}_{ex}} + \frac{\nu_c}{\nu_c-1} \frac{\sin^2\psi'}{\tilde{\lambda}_{ex}} + \frac{\cos\psi'_{ex}}{\tilde{\lambda}_{em}} \right]. \quad (5.18)$$

Referring back to equations (5.5) and (5.18), the only unknowns are the two principal strains, ε_1 and ε_2 . There are now two equations and two unknown principal strains. It is possible to determine the principal strains from these two equations. The theoretical principal strains are calculated from the theoretical maximum shear strain and matrix algebra. The matrix equation being solved is:

$$\begin{bmatrix} \gamma_{max,p} \\ \gamma_{max,o} \end{bmatrix} = \left[\begin{bmatrix} \frac{1}{\tilde{\lambda}_{ex}} - \frac{\nu_c}{\nu_c-1} \frac{\sin^2\psi'}{\tilde{\lambda}_{ex}} + \frac{\cos\psi'_{ex}}{\tilde{\lambda}_{em}} & -1 \\ \frac{\cos^2\psi'}{\tilde{\lambda}_{ex}} + \frac{\nu_c}{\nu_c-1} \frac{\sin^2\psi'}{\tilde{\lambda}_{ex}} + \frac{\cos\psi'_{ex}}{\tilde{\lambda}_{em}} & \frac{1}{\tilde{\lambda}_{ex}} - \frac{\nu_c}{\nu_c-1} \frac{\sin^2\psi'}{\tilde{\lambda}_{ex}} + \frac{\cos\psi'_{ex}}{\tilde{\lambda}_{em}} \end{bmatrix} \begin{bmatrix} \varepsilon_1 \\ \varepsilon_2 \end{bmatrix} \right]. \quad (5.19)$$

5.3 Measured Coating Calibration Parameters: ϕ and η

OSR data from the deflected specimens was used to calculate the coating calibration coefficients, η , first assuming the maximum shear strain based on linearized bending-beam theory (Eqs. 5.5 and 5.18). Polarization efficiency, ϕ , was modeled as the anisotropy value for the specimen (Eq. 3.12).

The polarization efficiency depends on the polarization retention of the luminescence and the substrate surface [12], which in turn affects the fitted value for the coating calibration coefficient. The calibration coefficient was calculated based on minimizing the least square error between experimentally-measured and theoretical OSR, calculated using equations (5.13, 5.15, 5.18). These parameters are unique to each specimen, and results for each specimen based on the measured OSR are listed in Table 5.1.

Table 5.1. Calibration coefficients for each specimen.

	2D		3D					
	Specimen 1		Specimen 1		Specimen 2		Specimen 3	
	Parallel	Oblique	Parallel	Oblique	Parallel	Oblique	Parallel	Oblique
ϕ	0.299	0.328	0.320	0.335	0.313	0.295	0.316	0.310
η	3815	4316	4989	4569	4734	4029	5098	4264
$\phi/\eta \times 10^4$	0.783	0.760	0.642	0.734	0.661	0.732	0.619	0.726

For low values of strain, ($\gamma \ll \eta$), equation (5.13) reduces to a linear relationship between the calibration coefficients and the shear strain,

$$OSR = \phi \frac{\gamma_{eff}/\eta}{1 + (\gamma_{eff}/\eta)^2} \approx \frac{\phi}{\eta} \gamma_{eff}. \quad (5.20)$$

The linearized calibration ratio, ϕ/η , is the slope of the OSR vs. shear strain graph for low strain values. These average calibration ratio for the three specimens is listed in Table 5.2. The calibration ratio depends on orientation: parallel or oblique. The 95% precision variance for each is small. Based on a two-sample t-test comparing the average parallel and oblique linearized calibration coefficient, the P-value is less than 0.002, indicating that the difference of the two measures is significant (rejection of the null hypothesis). Therefore, strain separation should be possible from the two OSR measures.

Table 5.2. 95% precision interval values for 3D specimens at parallel and oblique incidence angles.

	Parallel	Oblique
	ϕ/η $\times 10^4$	ϕ/η $\times 10^4$
Specimen 1	0.642	0.734
Specimen 2	0.661	0.732
Specimen 3	0.619	0.726
Avg	0.640	0.731
P95%	± 0.029	± 0.006

5.4 Rosette Strain Gage Data

A 45° rosette strain gage was applied to the compression side of one of the 3D tube specimens to validate the strain response. The gage was applied 17.78 cm from the point of application of the load. Additionally, each specimen had a uniaxial strain gage applied to the compression side for use with the triggering circuit. Strain readings were acquired from the rosette gage as well as the uniaxial gage.

The strain gage readings were much lower than that predicted by linearized beam theory. The major factor for this discrepancy was traced to the support frame used to clamp the specimens.

When the specimens are loaded, the frame does exhibit movement at the clamped end, allowing some rotation. This give in the frame causes less stiffness in the beam, and, hence, less force to be applied to the specimen to achieve the set deflection. This in turn causes the measured strains to be less than the theoretical shear strain for a fixed constraint beam. To correct for this difference, the strain along the x-axis for the specimen was estimated assuming a linear trend (beam theory) calibrated to the measured strain from the strain gage.

5.5 Experimental Results

5.5.1 Test Conditions

Tests were conducted in the Luminescent Imaging Lab where the specimen was mounted in cantilever fashion to a support frame. The CCD camera and LED light were mounted on a tripod approximately 1m across from the specimen. The camera was aligned and focused to capture images of the specimen. The f/stop of the camera was 1.2. Images were acquired in complete darkness with the exception of the excitation lamp.

In totality, three 3D square tubes and one 2D bar were tested. Tube specimens 1 and 2 were tested at 1 Hz frequency and tube specimens 2 and 3 were tested at 10 Hz. The 2D specimen was tested at 1 Hz and 10 Hz. Each specimen was imaged using two lamp orientations: normal and oblique. For the tube specimens, two sides were imaged at two lamp orientations. The cam deflects each specimen 0.3175 cm resulting in a theoretical force of 600.5 N applied to the end of the square tube specimens and a force of 42.3 N applied to the end of the bar specimen. However, based on strain measurements to calibrate the effect of constraint rotation, the applied forces are estimated to be 320 N for the tube specimens and 11.25 N for the bar specimen. An oblique excitation angle of $55^\circ \pm 2^\circ$ was used as the signal-to-noise ratio was shown to be

optimum at 53° [2]. The lamp and camera orientations are shown in Fig. 5.5a and the test instrumentation is shown in Fig. 5.5b.

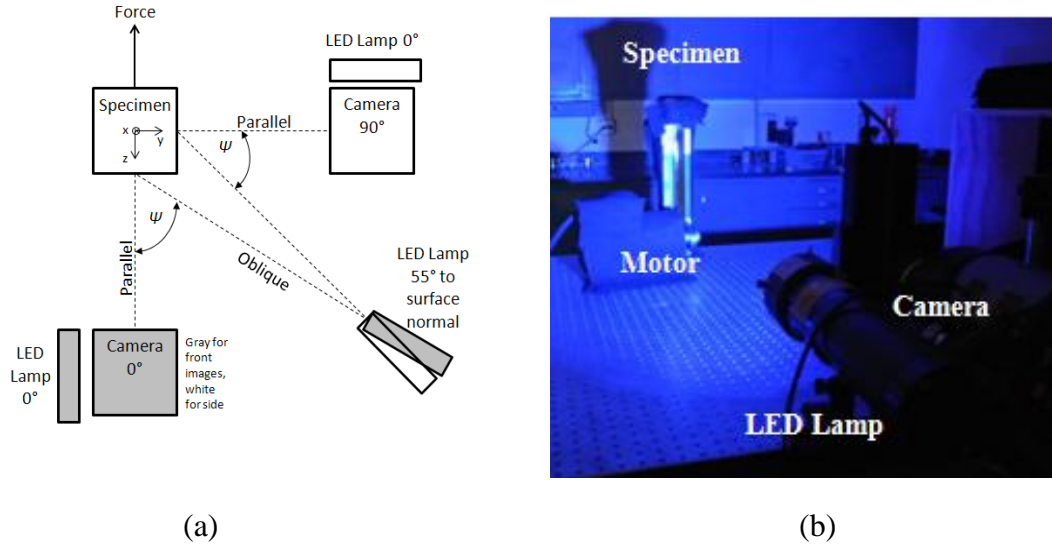


Fig. 5.5. Lamp, camera, and specimen positions and orientations (a) and test instrumentation (b).

The excitation source was circularly polarized blue light (wavelength 450 nm). The lamp flashed in synchronization with the frequency of the motor and flashed on at the desired trigger strain level. During the finite duration, the specimen is in motion and there is a slight change in strain. Thus, the captured strain state is slightly higher than the trigger level.

Table 5.3. Image acquisition parameters for various specimen types and load states.

Specimen Type	Frequency	LED Flash Time	Trigger Level	Change in Strain During Flash	Camera Exposure Time	Effective Excitation Time	Effective Strain State Acquired
[]	[Hz]	[ms]	[$\mu\epsilon$]	[$\mu\epsilon$]	[s]	[s]	[$\mu\epsilon$]
2D Bar	1	25 ± 1	500	43.2 ± 5	540	13.5	521.6 ± 2.5
	10	2.5 ± 0.1	500	43.2 ± 5	540	13.5	521.6 ± 2.5
3D Beams	1	25 ± 1	500	47 ± 5	540	13.5	523.5 ± 2.5
	10	2.5 ± 0.1	500	47 ± 5	540	13.5	523.5 ± 2.5

Images of the specimens under load were acquired near maximum deflection (Fig. 5.6). The unloaded images were acquired with the motor off and the cam in the undeflected position. For the unloaded case, the specimens were excited continuously with the LED lamp for an effective excitation time equivalent to the flashed state. A dark-field image was also obtained for each specimen to correct for any residual voltage in the camera pixels. This image was subtracted from each image to yield the corrected images.

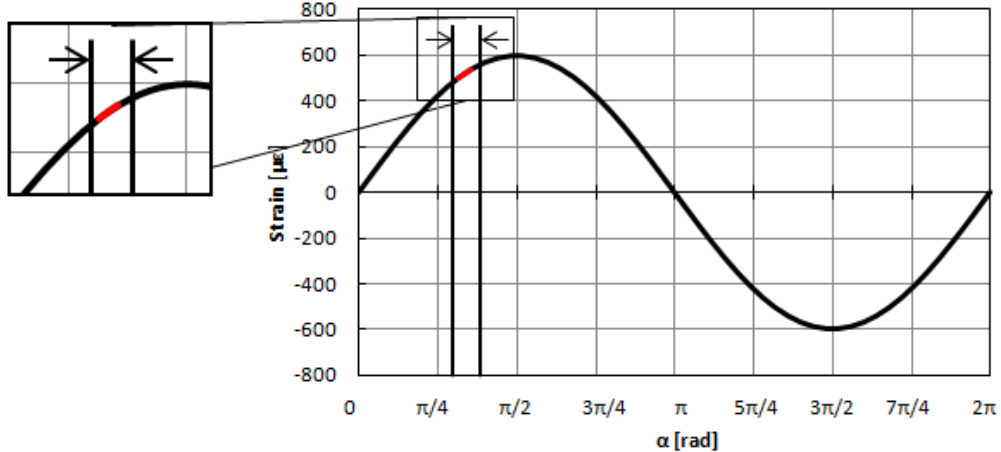


Fig. 5.6. Region of lamp flash on the sinusoidal strain response of cyclically loaded specimen.

5.5.2 Experimental OSR

Fig. 5.7 shows the processed, full-field OSR measurements for parallel and oblique cases on the front of the 2D specimen. The images show an applied false-color gradient where red indicates high strain and blue low strain. The OSR images of the 2D specimen show a high strain near the clamped end and low strain near the force end. In this case, the parallel incidence shows a higher optical strain response than the oblique case.

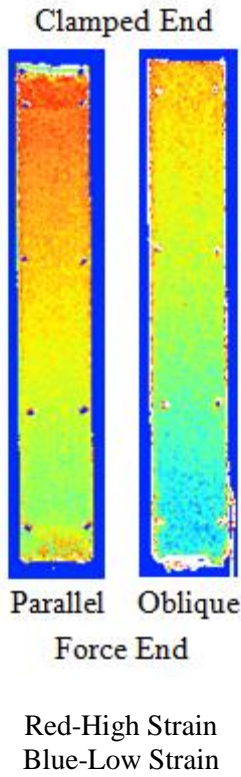


Fig. 5.7. Parallel and oblique OSR images for the 2D specimen.

OSR is related to strain, rather than the raw intensity of the images. It also depends on the ratio of the calibration coefficients, ϕ/η . In Table 5.1, the 2D specimen shows a higher ϕ/η value for the parallel data than oblique data. Conversely, the 3D specimens consistently show a higher ϕ/η value for the oblique data than parallel data. The coating and excitation parameter values used in equation (5.18) can affect the coating calibration coefficient and, thus, the ϕ/η and separated principal strain values. Table 5.4 shows typical coating and excitation parameter values, their estimated ranges, and the sensitivity of the experimental Poisson's ratio (ratio of in-plane maximum principal strains). The expected Poisson's ratio from this experiment is 0.33 (aluminum); however, the experimental Poisson's ratio is less than half of this value. Based on a sensitivity analysis, the largest contributing error source is the coating Poisson's ratio. A v_c value of approximately 0.73 yields the expected value for Poisson's ratio (0.33).

Table 5.4. Sensitivity of measured Poisson ratio to changes in coating and excitation parameters.

	n_c	θ	λ_{ex}	λ_{em}	v_c	v_{exp}	% Change from v
	[]	[deg]	[nm]	[nm]	[]	[]	[]
Typical Value	1.6	55	465	600	0.45	0.128	-
Range	± 0.1	± 3	± 5	± 5	± 0.05		
High End	1.7	55	465	600	0.45	0.123	-4.1%
Low End	1.5	55	465	600	0.45	0.134	4.6%
High End	1.6	58	465	600	0.45	0.133	3.7%
Low End	1.6	52	465	600	0.45	0.123	-3.8%
High End	1.6	55	470	600	0.45	0.128	-0.4%
Low End	1.6	55	460	600	0.45	0.129	0.4%
High End	1.6	55	465	605	0.45	0.128	-0.3%
Low End	1.6	55	465	595	0.45	0.128	0.3%
High End	1.6	55	465	600	0.50	0.153	20%
Low End	1.6	55	465	600	0.40	0.106	-17%

Fig. 5.8 shows the OSR images for parallel and oblique cases on the front (tension) and side (neutral axis) of the 3D specimen. As expected, the OSR is highest at the clamped end and lowest where the load is applied (Fig. 5.8a). The parallel case displays lower OSR than the oblique case. The OSR was expected to be higher for the parallel case [3]. In Fig. 5.8b, the side of the square tube is shown. In these images, the OSR changes from red or yellow to blue, and back to red or yellow, indicating the neutral axis.

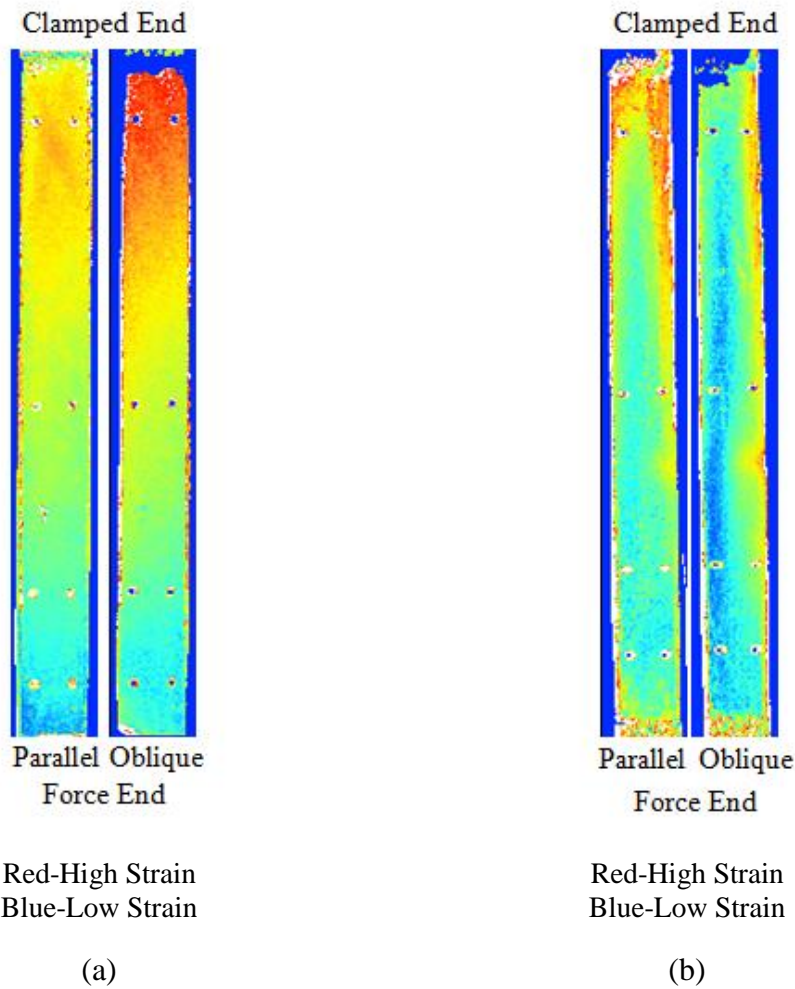


Fig. 5.8. OSR parallel and oblique images for (a) front and (b) side of a 3D specimen.

Fig. 5.9 shows the parallel and oblique centerline OSR for the 2D bars at maximum load for 1 Hz and 10 Hz frequencies. Shear strain was calculated using the difference between the x-direction and y-direction (transformed for oblique case) strains in the plane of propagation of light. The strain in the x-direction was corrected using a linear trend based on the uniaxial strain gage reading. The change in frequency shows a slight difference in the parallel case. For the oblique case, the two frequencies agree well with each other.

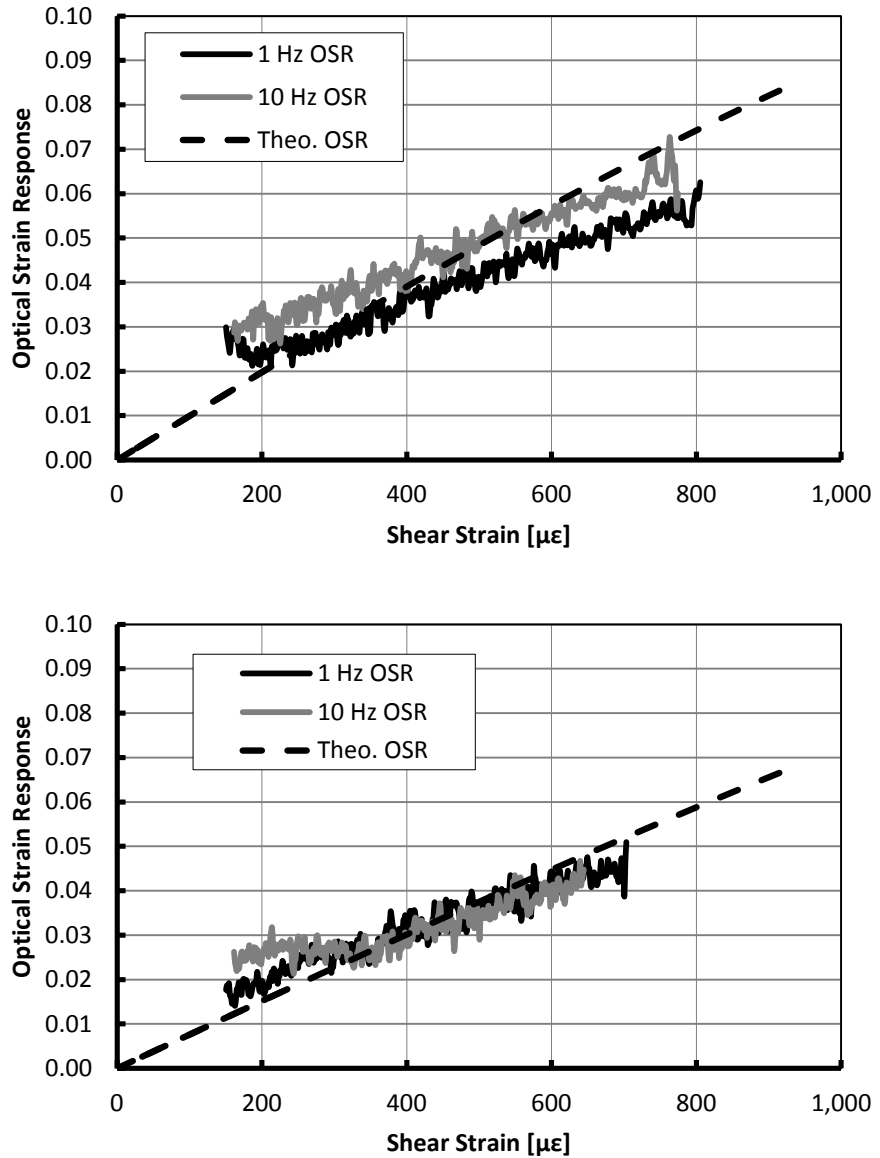


Fig. 5.9. Parallel (top) and oblique (bottom) excitation OSR response along the tension-side centerline of the 2D bar.

Fig. 5.10 shows the parallel and oblique OSR for the square tube beams at maximum load (deflection = 0.3175 cm) for 1 Hz and 10 Hz. Specimens 1 and 2 were loaded at 1 Hz and specimens 2 and 3 were loaded at 10 Hz. The OSR trends compare well with variance typical given the low-level of applied load. Particularly, the 1 and 10 Hz cases for specimen 2 overlap

nicely, indicating at least 10 Hz response without attenuation in sensitivity and, hence, quasi-static response.

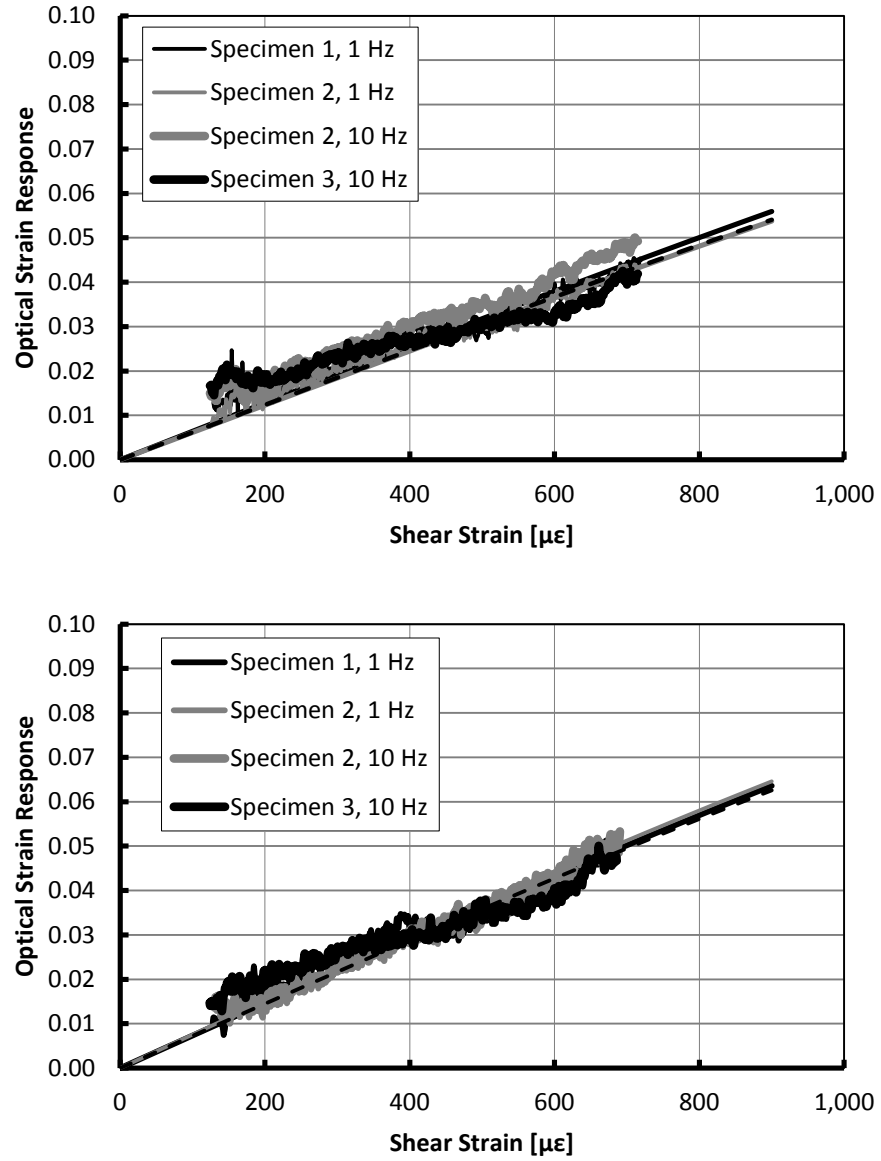


Fig. 5.10. Parallel (top) and oblique (bottom) excitation OSR response along the tension-side centerline of the square-tube beams.

5.5.3. Experimental Strain Separation

For strain separation, the experimental principal strains are compared to the theoretical principal strains once corrected for the clamp rotation. Fig. 5.11 shows strain separation conducted on the 2D bar specimen at 1 Hz frequency loaded to 11.25 N. The root-mean-square error in the principal strains relative to theoretical was $45 \mu\epsilon$ for ε_1 , and $57 \mu\epsilon$ for ε_2 . Results should show $\frac{\varepsilon_2}{\varepsilon_1} = -0.33$, but this is not the case. Again, this is possibly due to inaccurate coating parameters, particularly the coating Poisson's ratio, or errors in the strain separation and coating response modeling.

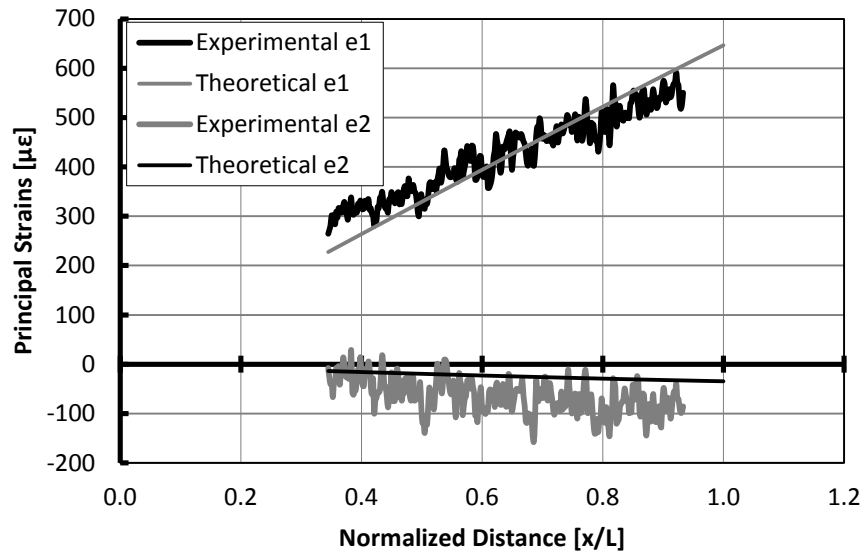


Fig. 5.11. Separated principal strains for the 2D bar specimen.

A theoretical model of the 3D beam was created using ABAQUS to compare the principal strains. The analysis used C3D8 elements. The C3D8 element is an 8-noded linear brick element (Fig. 5.13). Principal strains were calculated on the tension surface. The model was 11 elements wide and 120 elements long with 2 elements along the thickness. The principal strains in the

axial direction were determined at each 0.254 cm increment along the length of the beam to compare to the experimental and theoretical results.

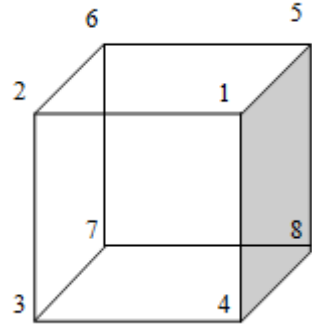


Fig. 5.12. 8-noded linear brick element.

The results of the ABAQUS method showed expected trends: the strain linearly increased towards the clamped end, the strain was relatively constant across the width of the specimen, and the results showed a neutral axis along the side of the beam. The FEA results may include some error due to the element type used and the application of the load (which was modeled as two equal forces). The load was applied over the width of the cam. Although modeling the load as two equal point loads could have introduced error locally, the error is negligible further away from the load (St. Venant's principle).

Fig. 5.13 shows the where the principal strain in the x, y, and z direction for the ABAQUS model was gathered from. In the axial direction, there is a color gradient where red is high tensile strain, green is approximately zero strain, and dark blue is high compressive strain. This shows what would be expected for a cantilever beam; high strain near the clamped end and low strain near the force end.

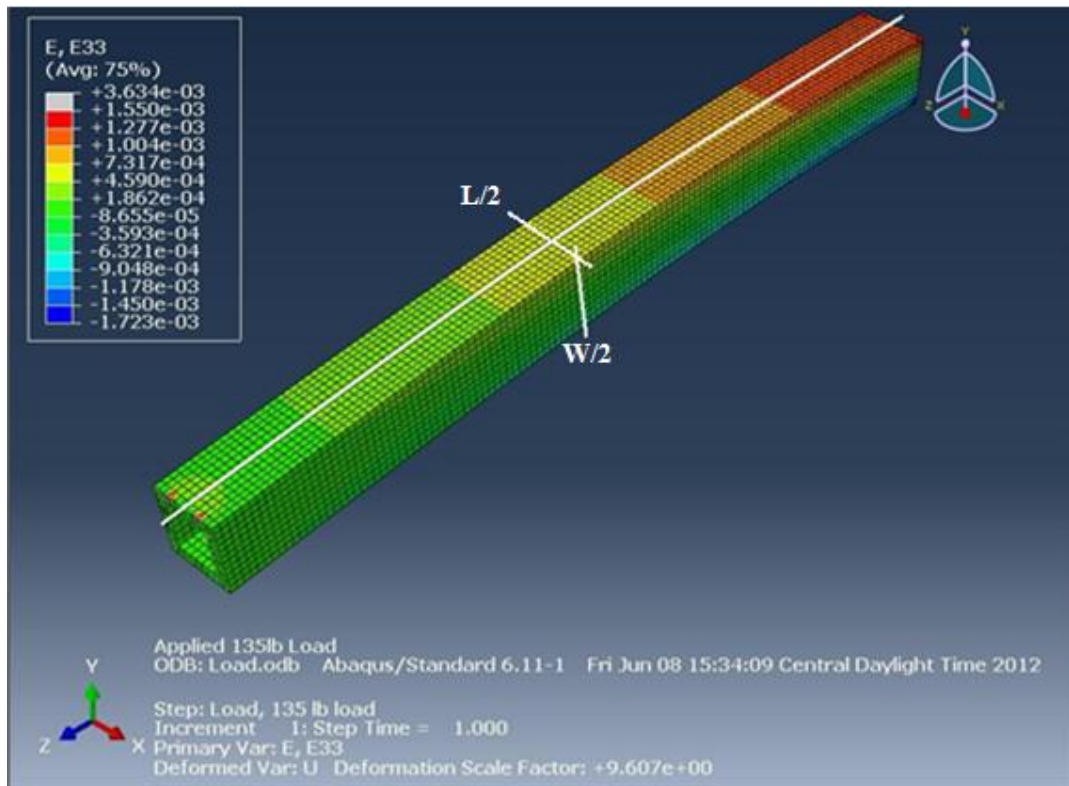


Fig. 5.13. Principal strain in the axial direction.

Fig. 5.14 shows the separated principal strains for a 3D specimen at 1 Hz. The root-mean-square error in the principal strains calculated through ABAQUS relative to the experimental results was $178 \mu\epsilon$ for ε_1 , and $61 \mu\epsilon$ for ε_2 . Both ε_1 and ε_2 from the FEA show a higher magnitude than experimental and theory. This is largely due to the give in the clamp as the FEA data was not corrected for this. The difference between the FEA and experimental ε_2 values is greater than that of ε_1 , meaning the ratio (or Poisson's ratio) of the two principal strain values did not stay constant between FEA and experimental. This is why the Poisson's ratio estimate is inaccurate.

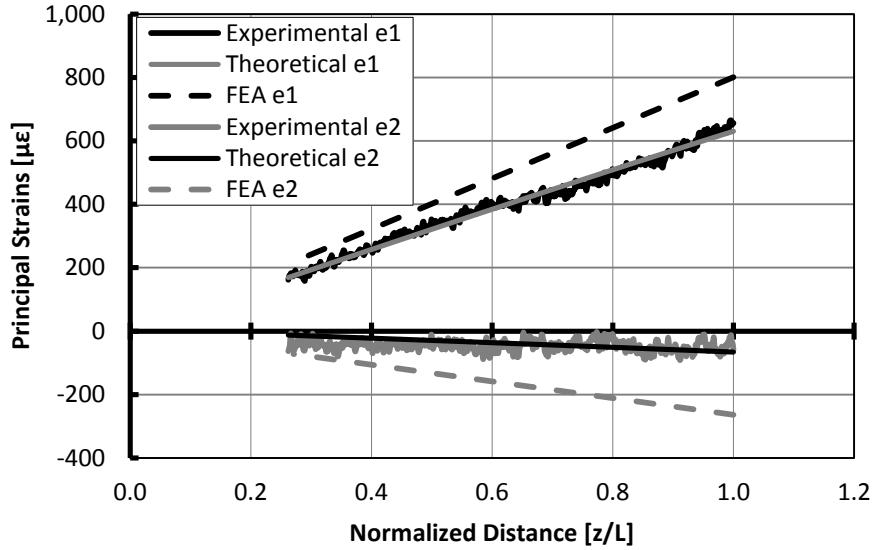
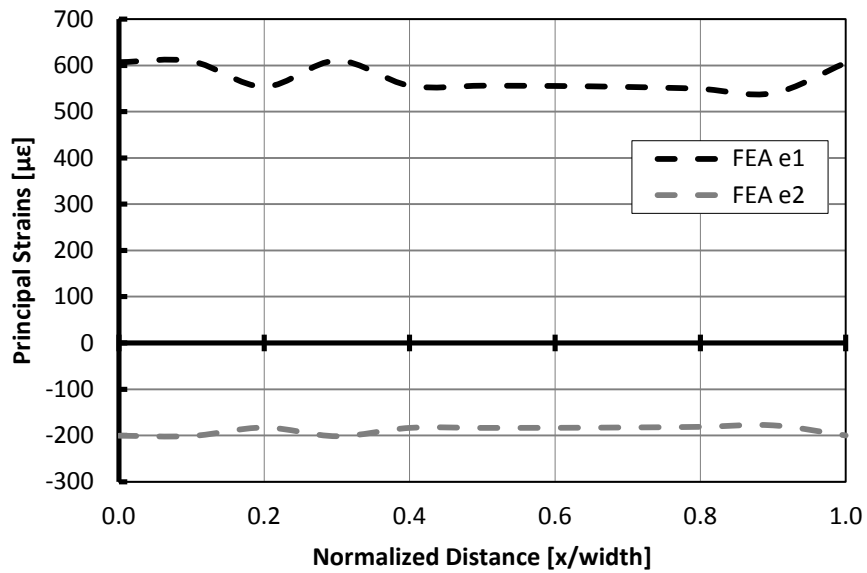


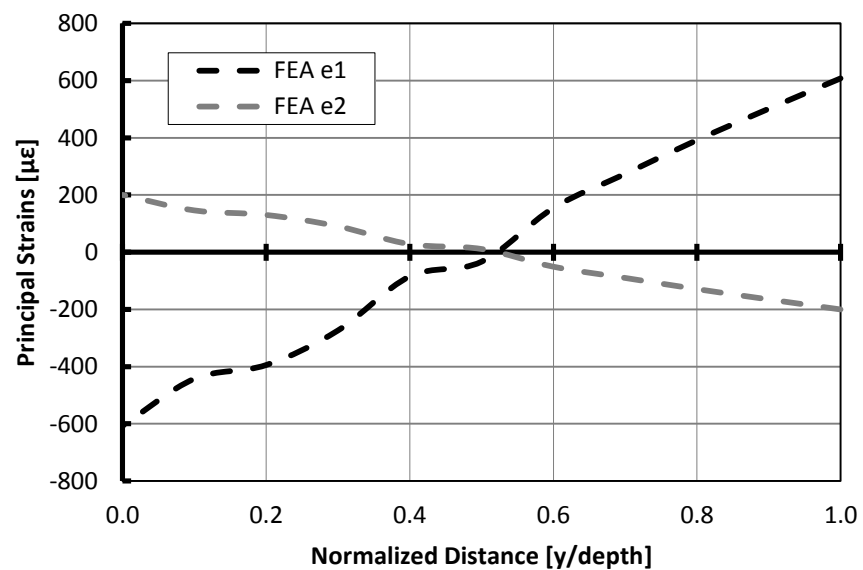
Fig. 5.14. Separated principal strains for the 3D beam specimen. Note: ABAQUS coordinate system used.

The strains are relatively constant in the x-direction (along the width) of the beam. Fig. 5.15a displays the principal strains along the width and the variance for ε_1 and ε_2 are both just 0.05 $\mu\epsilon$. At the midpoint of the length of the beam, the strain is also relatively constant along the width (Fig. 5.8a). The bar shows yellow-green color horizontally, with the edges showing red (higher strain). This red could be due to edge effects of the coating and should be neglected.

Along the depth of the beam (y-direction), the principal strains should be high, then close to zero as they pass the neutral axis, then back to an equal but opposite high value. Fig. 5.15b shows ε_1 and ε_2 starting around 600 $\mu\epsilon$ and -200 $\mu\epsilon$, respectively, crossing the x axis (indicating the neutral axis), and ending around -600 $\mu\epsilon$ and 200 $\mu\epsilon$, respectively. Fig. 5.8b shows the beam with a color gradient in the horizontal direction that ranges from yellow to blue and back to yellow again. Yellow indicates high strain, blue indicates strain close to zero. This confirms what we see in Fig. 5.15b. As both the experimental and FEA results show the strain returning to the value it was at y/depth = 0, there is negligible shear flow effects at y/depth = 0.



(a)



(b)

Fig. 5.15. Principal strains along (a) the width of the beam and (b) the depth of the beam.

5.5.5. Phase Results

Results from phase plots indicate principal strain directions. Fig. 5.16a displays a colored phase plot on the OSR image and Fig. 5.16b displays a black and white phase plot. The colored plot allows the OSR to be seen while the tick marks are easier to be seen on the black and white plot. As mentioned earlier, the red on the OSR indicates high strain while the blue indicates low strain. The tick marks indicate the axis of the principal strain, but not the actual direction. The knowledge behind the geometry of the specimen allows the direction to be specified. The specimen is known to be in tension on the front face and compression on the back face. Thus, the vertical tick marks indicate tension while the horizontal indicate compression.

Fig. 5.16a again displays high strain near the clamped end and low strain near the force end. On the side face of the specimen, the front face is now the left side of the image and the back face is the right. The OSR is seen to go from high strain to low strain and back to high strain on the back face. Fig. 5.16b shows the front face to have all vertical tick marks, showing the face to be in tension. The tick marks on the side face change from vertical on the left side to horizontal on the right side. The magnitude of the strain is theoretically the same on the front and back side of the specimen, but the principal strain direction has changed 180° , thus the tick marks have changed from vertical to horizontal.

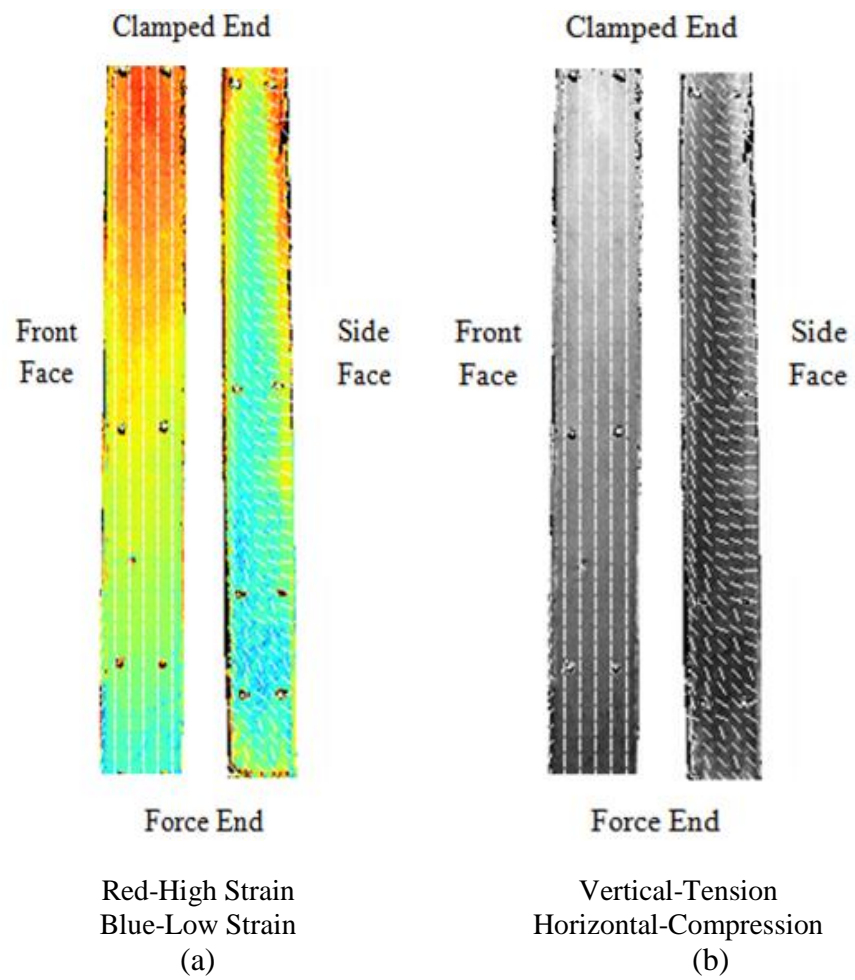


Fig. 5.16. Phase plots of the front and side face of a 3D specimen in (a) color and (b) black and white.

CONCLUSIONS

This research has focused on the dynamic application of the luminescent photoelastic coating technique. The dynamic application refers to a cyclic loading of the specimen rather than a transient. Two- and three-dimensional specimens were tested in bending and compared to theoretical expectations. The specimens were tested at 1 Hz and 10 Hz frequencies. Excitation was strobed in synchronization with the specimen while the camera shutter was left open. This allowed the specimen to be captured at a given stress state comparable to that expected when loaded statically.

This experiment completed three major tasks:

1. Successfully set up an experimental procedure to synchronize the excitation flashes with the cyclically loaded specimen.
2. Successfully performed dynamically loaded tests on 2D and 3D specimens at 1 Hz and 10 Hz frequencies.
3. Compared separated principal strains using LPC and oblique incidence of dynamically loaded specimens to theoretical results.

A triggering circuit allowed synchronization with the specimen to be possible. Prior to developing this hardware, software solutions were attempted. The software solutions did not allow for accuracy in synchronization, as a hardware solution did. The circuit was created to send a signal to the excitation source triggered by a strain gage located on the back of the specimen. By triggering at the same time in the specimen's sinusoidal path, the strain imaged remained constant over the imaging period. The pulse-width could be modified depending on the

resistor and capacitor values in the circuit. Pulse-widths of 25 ms and 2.5 ms were used for 1 Hz and 10 Hz, respectively.

Images of the 2D and 3D specimens were acquired for eight analyzer angles over a 180° rotation. Loaded and unloaded images were acquired for each incidence angle. The specimen was excited with parallel and oblique incidence on each of its imaged sides. The trigger circuit flashed consistently for the imaging period. Successful sets of images were acquired at 1 Hz and 10 Hz for 2D and 3D specimens.

Oblique incidence method was employed to separate principal strains. A two-sample t-test comparing the average parallel and oblique linearized calibration coefficient had a P-value of less than 0.002, signifying a significant difference in the two measures. This allowed strain separation to be performed. Once performed, the ratio of principal strains was lower than expected, possibly due to inaccurate assessment of the coating parameters. The root-mean-square error relative to theory in the principal strains for 1 Hz data were 13 $\mu\epsilon$ (ε_1) and 18 $\mu\epsilon$ (ε_2) on one of the 3D specimens, and 45 $\mu\epsilon$ (ε_1), and 57 $\mu\epsilon$ for (ε_2) on the 2D specimen.

REFERENCES

- [1] Drucker, DC. "Photoelastic Separation of Principal Stresses by Oblique Incidence." *Journal of Applied Mechanics, Trans. ASME.* Vol. 65. (1943): A156 - A160.
- [2] Takahashi, D and JP Hubner (2010) "Strain Separation on a Nonplanar Object using a Luminescent Photoelastic Coating" *Experimental Mechanics*, **50**[3]:365-375, DOI: 10.1007/s11340-009-9232-y
- [3] Esirgemez, E, and JP Hubner (2010) "Luminescent Photoelastic Coating Image Analysis and Strain Separation on a Three-dimensional Grid," *Optical Engineering*, **49**[9], DOI: 10.1117/1.3475946.
- [4] Aben, Hillar. "On the Role of T.J. Seebeck in the Discovery of the Photoelastic Effect in Glass." *Proc. Estonian Acad. Sci. Eng.*, Vol.13. Iss.4. (2007): 283-294.
- [5] Dally, JW and WF Riley. *Experimental Stress Analysis*, 4th ed. Knoxville, TN: College House Enterprises, LLC., 2007.
- [6] Lesniak, JR, and MJ Zickel. "Applications of Automated Grey-Field Polariscopic." *Proceedings of SEM Spring Conference: Houston, TX*, 1998.
- [7] Zandman, F, S Redner and JW Dally. *Photoelastic Coatings* Ames, IA: State University Press, 1977.
- [8] Wikipedia contributors. "Polarizer." *Wikipedia, The Free Encyclopedia*. Wikipedia, The Free Encyclopedia, 9 Jun. 2012. Web. 17 Jun. 2012.
- [9] Redner, SS. "New Oblique-Incidence Method for Direct Photoelastic Measurement of Principal Strains." *Experimental Mechanics*. Vol. 3. No. 3. (1963): 67 - 72.
- [10] Barone, S and EA Patterson. "Full-field Separation of Principal Stresses by Combined Thermo- and Photoelasticity." *Experimental Mechanics*. Vol. 36. No. 4. (1995): 318 – 324.
- [11] Takahashi and Hubner. "Optical Strain Response of a Luminescent Photoelastic Coating of a Sphere in Diametral Compression." *AIAA Student Paper, Region II Conference*, Apr. 2007.

- [12] Gerber, Daniel R., Hisham K. Ali and James P. Hubner. "Dynamic strain measurements with a luminescent photoelastic coating." Proc. SPIE 7981, 79815V (2011).
- [13] Gerber, Daniel, James Hubner. "A Factorial Design Experiment to Analyze the Optical Strain Response of a Luminescent Photoelastic Coating." AIAA Journal. Vol.48. No.10. (2010).
- [14] LEM2X-DM LED Light Source. Dayton, OH: Innovative Scientific Solutions, Inc.
- [15] Specification Sheet: Pixis: 1024, Princeton Instruments.
- [16] Specification Sheet: Achromatic Waveplates, Boulder, CO: Bolder Vision Optik, 2003.
- [17] Ali, Hisham. ““motor_run2.vi” Documentation.” Ref U of Alabama, 2011. Print.
- [18] Specification Sheet: LM741, Dallas, TX: National Semiconductor Corporation, 2004.
- [20] Specification Sheet: NE555, SA555, SE555 Precision Timers, Dallas, TX: Texas Instruments, 2004.
- [21] "DS1052E 50 MHz Digital Oscilloscope." *Rigol Beyond Measure*. N.p., n.d. Web. July-Aug. 2011. <<http://www.rigolna.com/products/digital-oscilloscopes/ds1000e/ds1052e/>>.
- [22] B&K Precision Instruction Manual for 1620A/1621A/1622A/1623A/1626A/1627A DC Regulated Power Supplies. Yorba Linda, CA: B&K Precision Corporation.
- [23] "SB-100P Super-High-Intensity UV Lamp." *Spectroline.com*. N.p., n.d. Web. 10 Jan. 2012. <http://www.spectroline.com/laboratory/lab_lamps_sb-100p.html>.
- [24] H&HS Single Action-External Mix-Siphon Feed Airbrushes. Chicago, IL: Passche Airbrush Company, 2007.
- [25] Hubner, JP, L Chen, Y Liu, K Schanze, J Nicolosi, P Ifju, and W El-Ratal (2005) "Characterization of a New Luminescent Photoelastic Coating," *Experimental Mechanics*, 45(2):137-143, DOI: 10.1007/BF02428186.